



RESEARCH ARTICLE

10.1002/2014JC010310

The effects of tides on the water mass mixing and sea ice in the Arctic Ocean

Maria V. Luneva¹, Yevgeny Aksenov², James D. Harle¹, and Jason T. Holt¹¹National Oceanography Centre, Joseph Proudman Building, Liverpool, UK, ²National Oceanography Centre, European Way, Southampton, UK

Special Section:

Forum for Arctic Modeling and Observing Synthesis (FAMOS): Results and Synthesis of Coordinated Experiments

Key Points:

- Tides have an important role in mixing in the Arctic
- This leads to a stronger reduction in sea ice
- A new pan-Arctic NEMO model is used to explore this

Correspondence to:

M. Luneva,
mane1@noc.ac.uk

Citation:

Luneva, M. V., Y. Aksenov, J. D. Harle, and J. T. Holt (2015), The effects of tides on the water mass mixing and sea ice in the Arctic Ocean, *J. Geophys. Res. Oceans*, 120, 6669–6699, doi:10.1002/2014JC010310.

Received 28 JUL 2014

Accepted 24 AUG 2015

Accepted article online 31 AUG 2015

Published online 15 OCT 2015

Abstract In this study, we use a novel pan-Arctic sea ice-ocean coupled model to examine the effects of tides on sea ice and the mixing of water masses. Two 30 year simulations were performed: one with explicitly resolved tides and the other without any tidal dynamics. We find that the tides are responsible for a ~15% reduction in the volume of sea ice during the last decade and a redistribution of salinity, with surface salinity in the case with tides being on average ~1.0–1.8 practical salinity units (PSU) higher than without tides. The ice volume trend in the two simulations also differs: $-2.09 \times 10^3 \text{ km}^3/\text{decade}$ without tides and $-2.49 \times 10^3 \text{ km}^3/\text{decade}$ with tides, the latter being closer to the trend of $-2.58 \times 10^3 \text{ km}^3/\text{decade}$ in the PIOMAS model, which assimilates SST and ice concentration. The three following mechanisms of tidal interaction appear to be significant: (a) strong shear stresses generated by the baroclinic clockwise rotating component of tidal currents in the interior waters; (b) thicker subsurface ice-ocean and bottom boundary layers; and (c) intensification of quasi-steady vertical motions of isopycnals (by ~50%) through enhanced bottom Ekman pumping and stretching of relative vorticity over rough bottom topography. The combination of these effects leads to entrainment of warm Atlantic Waters into the colder and fresher surface waters, supporting the melting of the overlying ice.

1. Introduction

Over the last decade, the Arctic Ocean (AO) has experienced the strongest reduction in sea ice cover seen over the last century. Since the beginning of the satellite record in the late 1970s, mean sea ice extent has declined in all seasons. The most notable change is in September, with a rate of about 13% per decade (National Snow and Ice Data Center, <http://nsidc.org/>) [Vihma, 2014]. Sea ice volume has also decreased at a rate of about $2.8 \times 10^3 \text{ km}^3/\text{decade}$ during the period 1979–2011, as estimated from the PIOMAS (Pan-Arctic Ice Ocean Model Assimilating System) model [Schweiger *et al.*, 2011]. The changes in Arctic sea ice have a strong impact on the ocean circulation in the AO through modification of the dynamical and thermohaline surface forcing of the ocean [e.g., Giles *et al.*, 2012], on the Arctic amplification via ice albedo and temperature feedbacks [Pithan and Mauritsen, 2014], and on weather at lower latitudes and, potentially, on the global climate [Francis and Vavrus, 2012; Screen, 2014]. However, these extraordinary changes in sea ice and subsequent feedbacks on the Earth's climate are neither fully understood nor well simulated in global climate models due to their coarse resolution and because they do not represent all key ocean processes.

Since continental shelves make up approximately 50% of the AO area, shelf-sea processes (such as ocean tides, land-fast ice-ocean interactions, coastal currents, downslope cascading, up/downwelling, and eddies) [Nurser and Bacon, 2014] have a substantial influence on the entire AO. These processes are generally not accounted for in either global or regional Arctic models, which do not have sufficiently fine horizontal meshes to resolve the required physical scales and sufficiently high vertical resolution to accurately simulate surface and benthic boundary layers. At present, none of the coupled ocean-atmosphere general circulation models (OA-GCMs) used in IPCC AR5 and only a few of the global or pan-Arctic models participating in the Forum for Arctic Ocean Modeling and Observational Synthesis (FAMOS; <http://www.who.edu/projects/famos/overview>) have sufficient resolution to account for shelf-sea physical processes. Those that do include FVCOM [Chen *et al.*, 2009] with 1–50 km resolution; the global 1/12° NEMO model [Bacon *et al.*, 2014; Duchez *et al.*, 2014], and the HYCOM Group's contribution (<http://hycom.org>) [Metzger *et al.*, 2014] with 3–5 km resolution in the AO. Of these, only FVCOM explicitly resolves

© 2015. The Authors.

This is an open access article under the terms of the Creative Commons Attribution License, which permits use, distribution and reproduction in any medium, provided the original work is properly cited.

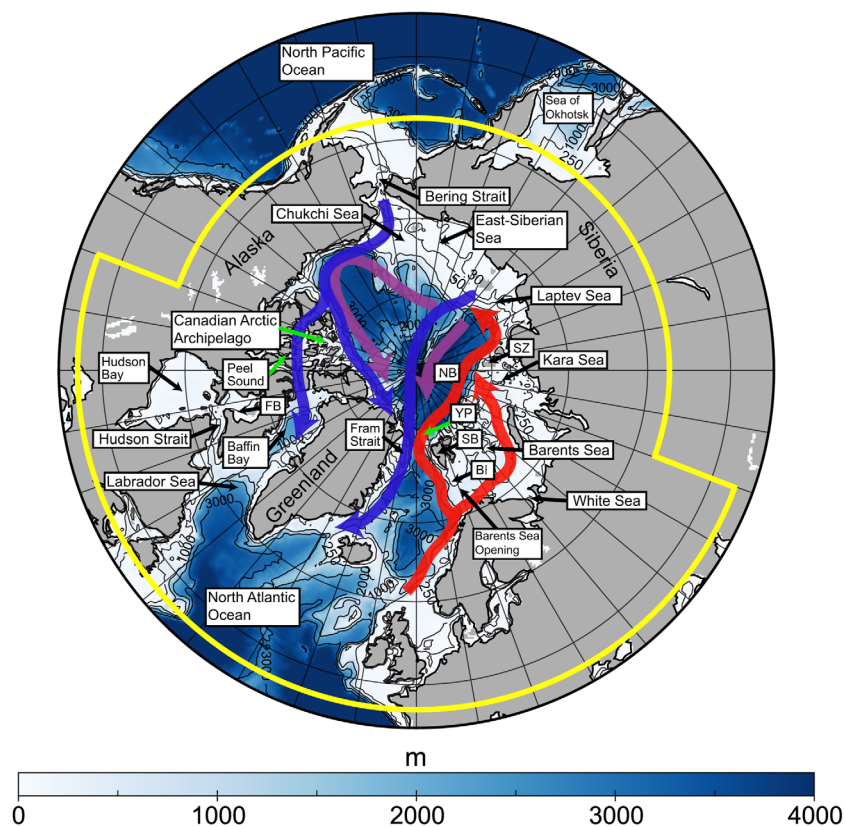


Figure 1. The NEMO model bathymetry (color) along with a schematic of the upper ocean circulation in the Arctic. Red and magenta arrows show Atlantic Water inflow and pathways of the cooled and freshened modified Arctic Atlantic Water; blue arrows show pathways of the polar waters. The lateral boundaries of the regional model domain are in yellow. FB denotes the Foxe Basin; BI, Bear Island; SB, Spitsbergen; YP, Yermak Plateau; NB, Nansen Basin; and SZ, Severnaya Zemlya.

tides and uses terrain-following coordinates, which are more effective at simulating dense water cascades and benthic boundary layers.

Astronomical tides are strong on the Arctic shelf with M2 amplitudes reaching 4.4 m in the Hudson Strait, 2–3 m in the White Sea and >1 m in the Canadian Archipelago (for geographical names see Figure 1). *Holloway and Proshutinsky* [2007] reviewed the observational and modeling evidence for the role of tides in the Arctic and presented arguments on why the “omission of tides from climate modeling can be particularly troubling.” They hypothesized that tidal-induced mixing in the AO plays an important role in the global conveyor belt. *Holloway and Proshutinsky* [2007] included a parameterization of tidal mixing near-bottom topography and tidal-induced divergence-convergence of ice in a coarse resolution (55 km) coupled ocean-ice general circulation model, and compared the results with and without tides on decadal time scales. Tidal currents in their study were derived from a barotropic ocean-ice coupled model with a grid spacing of 14 km [*Kowalik and Proshutinsky*, 1993, 1994]. The authors showed that the regions of strongest tidal dissipation are located along the western opening to the Barents Sea, above Yermak Plateau and over Eurasian continental shelf slopes in the Barents, Kara and Laptev Seas, thus mapping well onto the pathway of the Atlantic Water (AW) inflow in the AO. They suggested that tides can result in AW ventilation and modification via the mixing of this water mass with overlying polar waters, affecting the Arctic extension of the conveyor belt and potentially changing the Arctic and global climate.

In contrast, comparatively low mixing due to double diffusion processes is found in the Canadian Basin [*Padman and Dillon*, 1987; *Timmermans et al.*, 2008] and in the Eurasian Basin [*Perkin and Lewis*, 1984; *Ander-son et al.*, 1994; *Rudels et al.*, 1999]. This results in very moderate heat fluxes in the AO (0.05–0.3 W m⁻²) and cannot explain the observed rate of modification of AW along Eurasian shelf break [*Lenn et al.*, 2009; *Polyakov et al.*, 2012]. *Padman and Dillon* [1991] first identified tides as the main energy source that supports the enhanced dissipation rate of turbulence over steep topography. This is also supported by recent

microstructure measurements of turbulent kinetic energy dissipation [Rippeth *et al.*, 2015]; tidal effects have been found to be capable of generating heat fluxes of more than $35\text{--}50\text{ W m}^{-2}$.

To our knowledge, with the exception of a regional study by Postlethwaite *et al.* [2011], there have been no previous modeling studies that consider the effects of tides on the AO by comparing numerical simulations with and without explicitly resolved tides. Although we note that Koentopp *et al.* [2005] and Makinson *et al.* [2011] considered similar issues for the Weddell Sea in the Antarctic. In this paper, we focus on ocean tides and their effects on the hydrography and sea ice in the AO using a novel pan-Arctic sea ice-ocean coupled model configuration. The configuration is based on the NEMO model (Nucleus for European Modelling of the Ocean) [Madec and NEMO Team, 2008]. It employs realistic high-frequency atmospheric forcing from a reanalysis and explicitly simulates tidal dynamics and processes in the benthic and ocean-ice boundary layers. The model resolution (10–15 km) is internal tide and eddy-“admitting” (i.e., resolving explicitly large eddies) [e.g., Penduff *et al.*, 2007] in the deep AO, but not sufficient to resolve these on the shelf where the baroclinic Rossby radius is of order 1–7 km [Nurser and Bacon, 2014]. The goal of this paper is to identify key tidal-driven physical mechanisms that affect mixing and water mass transformation in the AO. While this present study does not examine the role of internal tides in full, it contributes to our understanding of the climate scale effects of tides on the water mass formation and ice evolution in the AO. By exploring key dynamical processes and examining the AO variability on decadal time scales (1978–2007), we demonstrate that tides make a significant contribution to the transformation of Arctic water masses and contribute to the reduction in sea ice.

The paper is organized as follows. In section 2, we summarize the effects of tides on mixing in the AO and the observational evidence, and formulate the hypotheses addressed in the study. In section 3, we describe the numerical model and experiments. Results from the tidal simulations are presented in section 4. Section 5 discusses the results of 1 year long simulations, demonstrating the immediate effects of tides, with section 6 expanding to the decadal effects of tides. Section 7 concludes the paper and summarizes the findings of the study.

2. Effects of Tides in the AO: Observations and Hypotheses

There is substantial observational evidence of the effects of tides on the hydrophysical fields in the high-latitude oceans with sea-ice cover. We separate these effects into four main groups, described in the sections 2.1–2.4.

2.1. High-Frequency Ice Oscillations

High-frequency fluctuations of ice motion and deformations due to inertial and tidal oscillations were described by Hunkins [1967] and have been identified in drifting buoy data obtained in the AO during summer months [Hibler *et al.*, 1974; Colony and Thorndike, 1980; Pease *et al.*, 1995]. Heil and Hibler [2002] show substantial variability of sea ice at a semidiurnal period during all seasons. Kowalik and Proshutinsky [1994] suggested that the persistent divergence and convergence of sea ice might enhance heat loss from the ocean to the atmosphere, which may in turn lead to increased formation of young ice in the cold seasons. They estimated the young ice formation rate to be 3 cm/d in open leads. Kwok *et al.* [2003] found a persistent detectable level of oscillatory ice motion in the AO with semidiurnal period in high-resolution satellite data acquired in winter. They estimated a potential growth of 0.1 m of ice during winter due to the opening and closing of ice. This constitutes approximately 20% of the mean annual basal growth of the thick ice pack in the central Arctic (0.5 m). Padman *et al.* [1992] estimated the tidal stress divergence at the ice underside as being an order of magnitude greater than the wind stress divergence acting on the top ice surface. Mack *et al.* [2013] extracted tidal signals from satellite data in the Ross Sea and found tidal amplitudes of ice concentration above 0.2 for diurnal harmonics. Numerical studies (Koentopp *et al.* [2005] in the Antarctic Ocean and Holloway and Proshutinsky [2007] in the AO) emphasize the competing role of tide-forced periodic ice divergence: in summertime, the ocean receives higher insolation due to opening/closing of leads, increasing ice melt; in wintertime, the same process leads to growth and ridging of new ice.

2.2. Benthic and Surface Boundary Layer Mixing

An increase in shear stress and vertical viscosity/diffusivity in the bottom boundary layer has been commonly observed in strong tidal flows [Robertson *et al.*, 1998]. The presence of ice introduces a second

boundary layer at the ice-ocean interface [e.g., Nøst, 1994]. In the AO, the three most energetic semidiurnal harmonics reach their critical latitudes (hereafter λ_{cr}), where frequencies of semidiurnal tides equal the inertial frequency (70°58" for N_2 , 74°28" for M_2 , and 85°40" for S_2). Observations show that in a water column with near homogeneous viscosity, the tidal current near λ_{cr} becomes strongly depth dependent with strong shear stresses and thick benthic and surface boundary layers [Prandle, 1982; Nøst, 1994; Furevik and Foldvik, 1996; Howarth, 1998]. Observations at the Ronne Ice Front in the Weddell Sea [Makinson et al., 2002, 2006] demonstrated that the combined upper and lower boundary layer in winter can occupy the entire water column within 100–200 km of λ_{cr} . Similar results have been found for the semidiurnal component of currents from observations in the Canadian Arctic in Peel Sound at 73.5°N [Prinsenbergh and Bennett, 1989]. These effects are strong even in more southerly latitudes, 1000 km from critical latitudes (in Hudson Bay at approximately 63°N), where differences in tidal and inertial frequencies are about 0.1f.

2.3. Baroclinicity and Internal Tides

The baroclinicity of tides relates to both the interaction of stratification with the tidal boundary layers, resulting in seasonal vertical variation in amplitude and phase [Howarth, 1998], and to internal tides. Both mechanisms may contribute to larger tidal shear and enhanced mixing within the pycnocline, although they differ in origin and characteristics. Near the critical latitudes, the Ekman layer tends to span the entire water column in a layer with approximately vertical constant viscosity, K_m . Where a pycnocline is present, so K_m is depth dependant, an anticyclonic (clockwise in the Northern Hemisphere) component of the tidal current generates an extremely strong shear in the layer of reduced K_m [Maas and van Haren, 1987; Souza and Simpson, 1996; Makinson et al., 2006]. Internal tides, generated through interactions between the barotropic tides and bottom topography, result in the vertical displacement of isopycnals. The breaking and shear instability of internal waves also contributes to mixing within the pycnocline [Vlasenko et al., 2003]. Internal waves with diurnal, near-inertial and quarter-diurnal periods have been observed near the Yermak Plateau [Padman and Dillon, 1991; Fer et al., 2010], at moorings in the Beaufort and Chukchi Seas [Rainville and Woodgate, 2009; Martini et al., 2014] and in the Canada Basin during the Surface Heat Budget of the Arctic Ocean (SHEBA) Programme [e.g., Pinkel, 2005] and from the Ice-Tethered Platform (ITPs) [e.g., Dosser et al., 2014]. Internal waves may increase mixing and modification of the AW [Padman et al., 1992; Pinkel, 2005]. In the deep part of AO (about 1000 m), Padman and Dillon [1991] estimated the mean diapycnal heat flux to be about 30 W m^{-2} above the Atlantic layer core, an order of magnitude larger than that in the surrounding much deeper waters near the Yermak Plateau. Estimates by Fer et al. [2010] for the deep ocean give $15\text{--}25 \text{ W m}^{-2}$. Lenn et al. [2011] observed in the shallow, strongly stratified Laptev Sea, a strong tidally induced shear (between 3×10^{-2} and $10 \times 10^{-2} \text{ s}^{-1}$) at the depth of the halocline (20–30 m) and concurrent bursts of intense mixing. They explained these intense bursts of shear and mixing using results from a 1-D model [Burchard and Rippeth, 2009], where extreme shear was generated when tidal surface currents were aligned with the surface currents, driven by ice motion. Strong baroclinicity of tides and shear in the strongly stratified halocline layer in the eastern Laptev Sea shelf has been detected by Dmitrenko et al. [2012]. They observed sporadic occurrence of a nearly homogeneous layer inside the halocline and consequent reduction of gradient Richardson number. Janout and Lenn [2014] observed an increased dissipation rate at the halocline associated with tides in the Laptev Sea.

2.4. Residual Currents and Rectification

Field measurements and laboratory experiments [Vinje et al., 1989; McClimans and Nilsen, 1993] show that the ice floes around Bear Island in the Barents Sea are trapped by clockwise circular motions, which have been explained by Kowalik and Proshutinsky [1995] through the generation of topographically trapped waves and residual circulation (rectification) reaching 8 cm s^{-1} . Rectification refers to the generation of time-independent currents by tidal flows across depth contours or past coastal headlands [Zimmerman, 2014; Huthnance, 1981]. In the presence of friction at the seabed or an ice interface, periodical motions transfer energy to bottom and ice-ocean shear stresses with a substantial nonperiodic component and induce a time-independent component in the Ekman currents. Irregularities in the velocity and bottom shear stresses over a varying topographic relief generate vorticity and vertical motions that result in ageostrophic circulations and either geostrophic upwelling or downwelling of isopycnals. The efficiency of energy transfer from tidal currents to the rectified circulation increases when the characteristic length scales of depth variation match the range of horizontal tidal movement [Zimmerman, 1978, 1980; Loder, 1980; Robinson, 1981] (see also contemporary review Polton [2015]). Kowalik and Proshutinsky [1994, 1995]

estimated residual currents of $0.08\text{--}0.1\text{ m s}^{-1}$ in some regions of the Arctic Ocean. *MacAyeal* [1985] explained the basal melting in the Ross ice shelf through a supply of warmer water by the rectification of currents (as a result of tidal interactions with the topographic and under ice shelf relief). *Padman et al.* [1992] examining the topographic enhancement of diurnal tides in Yermak Plateau, suggested that rectified along-slope flow by the combination of cross-slope tidal currents, planetary vorticity, and bottom friction may explain the filament of the AW current advected clockwise.

2.5. In This Study We Consider the Following Hypotheses

- A. Periodic ice motions induced by ice-ocean shear stresses result in the opening and closing of leads, thus affecting the ice formation and heat fluxes between the ocean, ice, and atmosphere.
- B. The clockwise component of tidal currents result in thicker surface and bottom boundary layers and so enhance the exchange between the halocline and the warm Atlantic layer.
- C. Critical latitude effects result in strong baroclinicity of tides and generate layers with strong shear in the interior at or below the base of the mixed layer.
- D. Residual tidal circulation induced by nonlinear advection or tidal shear stresses leads to intense quasi-steady vertical motions and contributes to modification of water mass properties.

Our model does not resolve internal tides on the shelf, so we restrict our consideration of the baroclinicity of tides to that due to the interaction of boundary layers and stratification.

3. Model Setup and Numerical Experiments

We use the NEMO ocean model [*Madec and NEMO Team*, 2008], which is a nonlinear primitive equation, three-dimensional model, coupled to the Louvain-la-Neuve Ice Model version 2 ice model (LIM2). LIM2 employs Semtner's thermodynamics [*Fichefet and Maqueda*, 1997] and dynamics with elastic-viscous-plastic sea ice rheology (EVP) [e.g., *Hunke and Dukowicz*, 1997], implemented on a C-grid [*Bouillon et al.*, 2009]. The global $1/4^\circ$ configuration of NEMO with LIM2-EVP has been extensively tested in the FAMOS project to verify model skill in simulating the AO circulation and sea ice [e.g., *Jahn et al.*, 2012; *Johnson et al.*, 2012].

NEMO has been adapted to include shelf-sea and shelf-break processes [*O'Dea et al.*, 2012], providing a realistic application to broad tidally active continental shelf regions. These adaptations include a nonlinear free surface formulation with variable volume, mode-split explicit time stepping, the Generic Length Scale turbulence model [*Umlauf and Burchard*, 2003], a semiimplicit scheme for bottom friction and generalized vertical coordinates. The global NEMO configuration has a tripolar model grid, with the model poles at the geographical South Pole, in the Canadian Arctic and Siberia, with a "seam" or "north fold" between the latter two. In the regional, pan-Arctic configuration considered here (Figure 1), we use an extraction of the mesh and topography from the global $1/4^\circ$ NEMO configuration [*Madec and NEMO Team*, 2008]. In this model setup, the northernmost part of the tripolar grid is used, with a reindexing of the grid to a rectangular model domain without the "north fold," thus creating a seamless model grid. As a result, there are two open liquid boundaries: in the Bering Sea, located at 57°N and in the Atlantic Ocean near 48°N (Figure 1). The nominal $1/4^\circ$ resolution corresponds to 15 km in the central basin, 10 km on the Siberian shelf, and down to about 6 km and finer in the Canadian Arctic Archipelago. The model uses a new generalized hybrid vertical coordinate [*Shapiro et al.*, 2013] with 50 vertical levels: 20 terrain-following s -levels in the upper 300 m and 30 partial-step z -levels below. The s -levels are evenly distributed in shallow regions (shallower than 50 m) and stretched in the central water column in deeper water while maintaining high resolution in the upper and lower boundary layers. Vertical mixing in the AO is an order of magnitude smaller than elsewhere in the global ocean, with a significant fraction of total diapycnal mixing in the AO being attributed to double-diffusive processes that are not currently present in this model. To guarantee the small background vertical mixing (artificial and modeled), we employ the Piecewise Parabolic Method [*Colella and Woodward*, 1984; *James*, 2000] for vertical advection for tracers and set a background vertical diffusivity of $\sim 10^{-6}\text{ m}^2\text{ s}^{-1}$. For vertical diffusivity/viscosity parameterization we used (k-e) model with Kantha and Clayson [1994] structural functions, which we found less diffusive between Generic Length Scale options, available in NEMO module. The lateral mixing is set by a Laplacian geopotential operator and uses the Smagorinsky parameterization. Exchanges of momentum, heat, and

freshwater/salt fluxes at the ice-ocean interface are computed every baroclinic time step, which is 600 s in the model.

Initial and open boundary conditions include temperature, salinity, and slow-varying component of sea surface elevation derived from 5 day mean fields from a global $1/4^\circ$ NEMO simulation without tides [Johnson *et al.*, 2012]. We add tides by specifying geopotential tidal forcing with 15 constituents and lateral boundary conditions for 9 tidal harmonics (barotropic velocities and sea surface elevations) from the $1/4^\circ$ resolution inverse tidal model TPX07.2 [Egbert and Erofeeva, 2002]. Surface air-ice and air-ocean fluxes are calculated from the Common Ocean-Ice Reference Experiments (CORE) atmospheric boundary layer formulae [Large and Yeager, 2004] using atmospheric fields from the DRAKKAR Forcing Set v5.1.1 (DFS5.1.1). These are supplied at 3 h intervals and 0.7° spatial resolution [Brodeau *et al.*, 2010]. Climatological (mean seasonal cycle) continental river runoff is used, as described by Barnier *et al.* [2006].

Two numerical simulations, one with, and another without tides (hereafter “T” and “NT”) are performed. Both the simulations begin on the 15 January 1978 and have a “spin-up” for 1 year forced with the DRAKKAR Forcing Set (DFS) v4.1 atmospheric forcing [Brodeau *et al.*, 2010]. Then, the integrations continued for 1979–2007 using DFS v5.1.1 forcing. This period is used for the analysis.

Water masses of the AO change significantly during the 29 years of simulation, and nonlinear interaction of advection, mixing, currents, and ice formation takes place. This makes attribution of the dominant processes difficult. To isolate the immediate effects of the tides, we consider an additional 1 year long spin-down model experiment. In this experiment, the model is run for 1 year (1978) with tides and then run through 1979 without tides. The tidal energy completely dissipates after a month and then we compare the results with the original solution with tides for 1979. We use these to explore the four hypotheses identified in section 2.5.

4. The Simulation and Diagnostics of Tidal Processes

The model reproduces the six main tidal harmonics (M2, S2, N2, K1, O1, and S1) reasonably well in comparison with the 5 km resolution inverse barotropic Arctic Ocean model AOTIM-5 [Padman and Erofeeva, 2004] and the high-resolution FVCOM [Chen *et al.*, 2009] model (see Figures 2a and 2b for amplitude and phase of M2 and K1 harmonics). It runs stably with tidal elevations exceeding 4.5 m and maximum tidal currents of up to 3 m s^{-1} . The spatial distribution of the amplitude and the locations of amphidromes for S2 and N2 harmonics (not shown) are very similar to those of M2, but with smaller maximum amplitudes: about 1 and 0.55 m, respectively. Figure 2c shows a comparison between model M2 amplitude for 1979 and both model [Padman and Erofeeva, 2004] and in situ observations [Kowalik and Proshutinsky, 1994]. For the latter case, we only include data where the distance to the closest model sea point does not exceed 10 km (207 values). The mean error between model and observations is 0.036 m and RMS is 0.18 m. These results are satisfactory given the model resolution [see Padman and Erofeeva, 2004, table], and that the grid has not been refined for tidal simulations. Moreover, tidal amplitudes and phases exhibit strong seasonal variability, first documented for velocity by Howarth [1998] for European shelf seas and for the AO by St-Laurent *et al.* [2008]. Ice conditions and stratification affect the tidal amplitudes, with relative anomalies (defined as the maximum of seasonal or interannual difference divided by mean amplitude) of up to 0.35–0.50 (Figures 2d and 2e). The strongest seasonal and interannual variability is observed in the Bering Strait, Chuckchi Sea, East-Siberian Sea, and Laptev Sea. For the latter, strong seasonal and interannual variability of tidal currents has been observed by Janout and Lenn [2014].

4.1. Tide-Ice Interaction

To verify that the model can simulate the present state of sea ice, we compare the ice concentration in the simulation with tides and that from the HadISST observational data set, described by Rayner *et al.* [2003] and extended to 2007. The observational and model data are averaged for the winter (DJF) and summer (JJA) months for 1978–2007 (Figure 3). The HadISST data are based on the advanced very high-resolution radiometer (AVHRR) satellite observations. Generally, the model concentration fields are close to the observed (more so in the case of the tidal simulations), although there are biases in the model. The model overestimates wintertime sea ice concentration in the Barents and Greenland Seas and in Fram Strait, whereas it underestimates sea ice concentration in Baffin and Hudson Bays (Figures 3a and 3b). In summer,

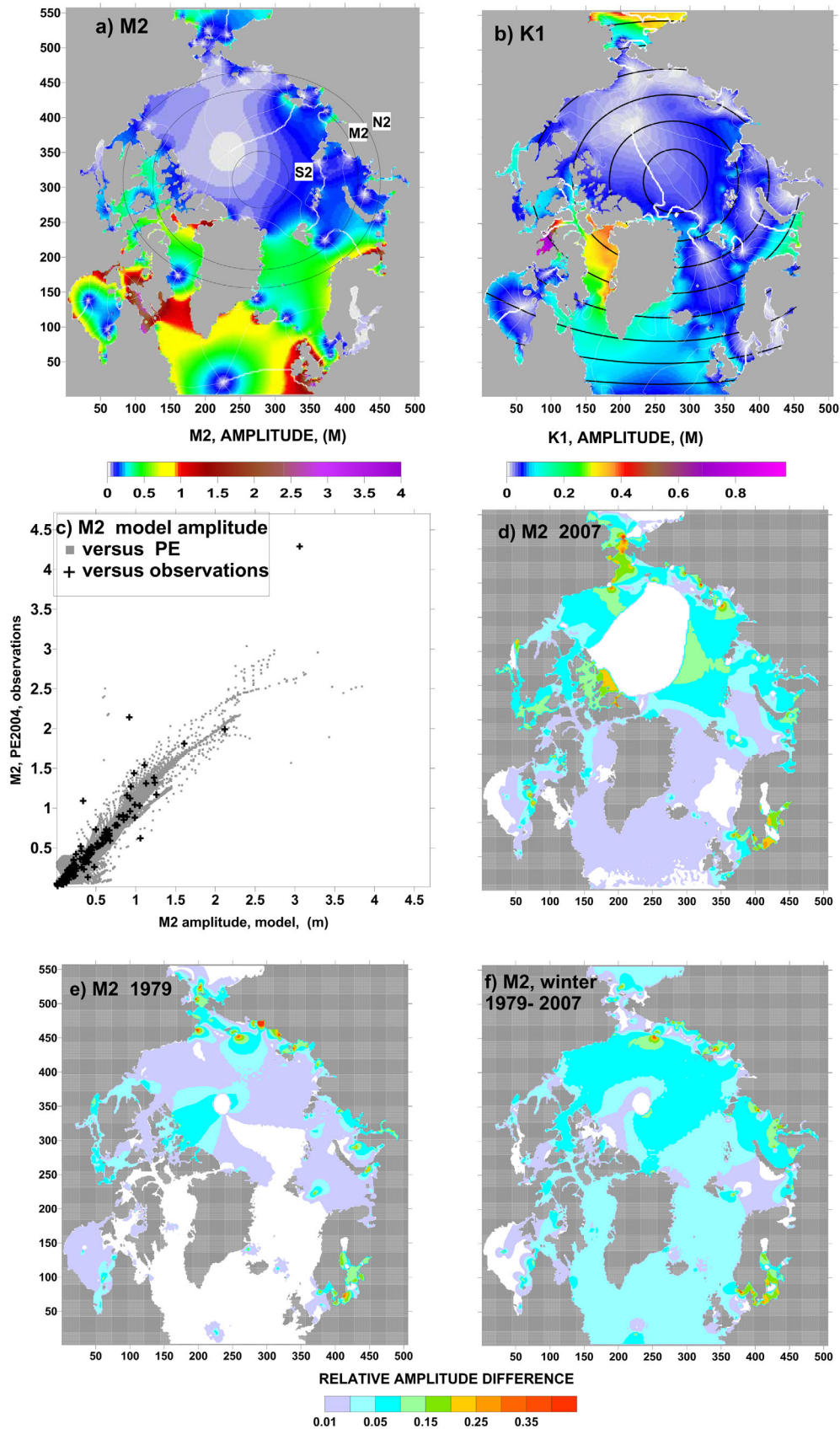


Figure 2.

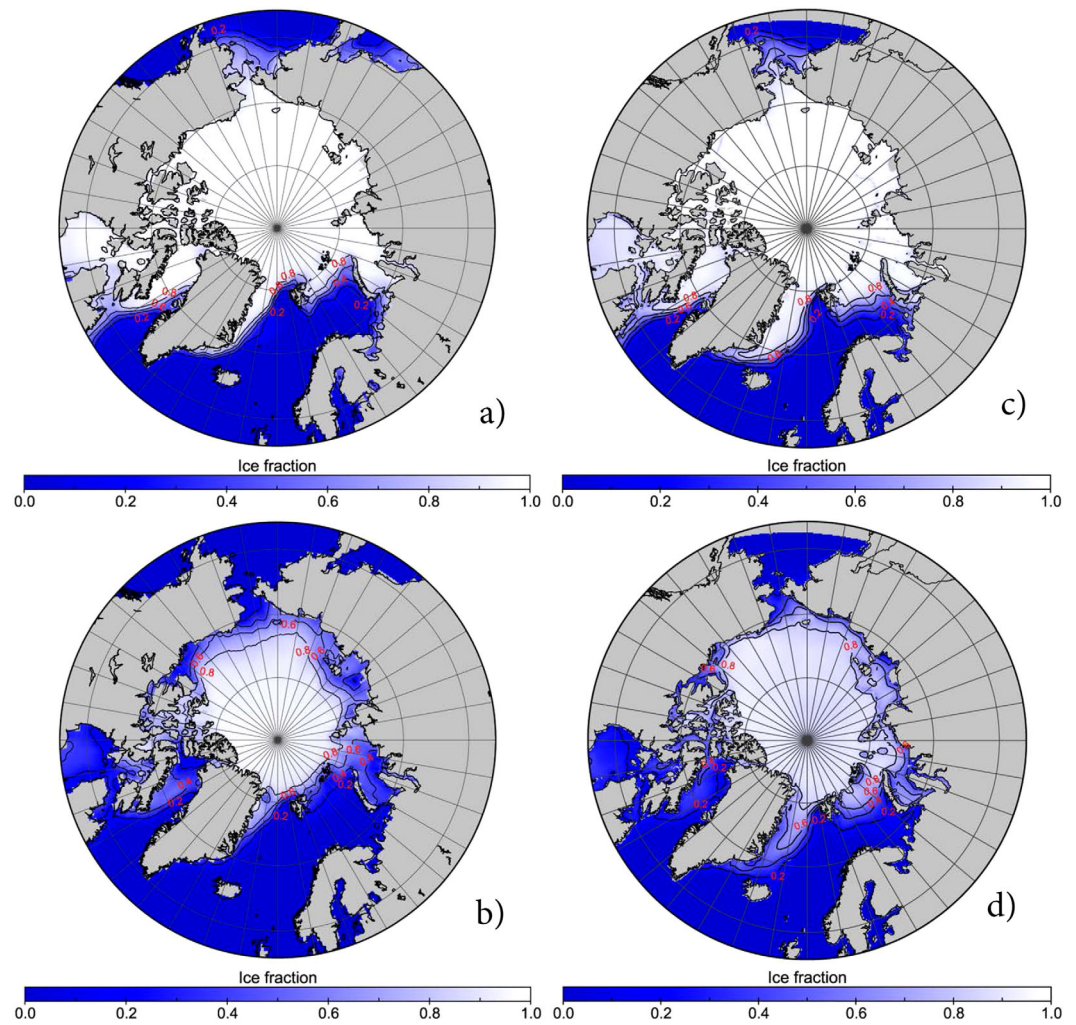


Figure 3. Ice concentration averaged over 30 years. (a, b) HadISST data set winter months (DJF) and summer month (JJA) correspondingly. (c, d) The same for model simulations with tides.

the modeled sea ice concentrations are higher than observed in the Barents, Kara, and Greenland Seas, and also along the Alaskan shelf. These biases, however, typically do not exceed 15% and are not detrimental for the presented analysis. Modeled mean summer ice concentrations are slightly higher (by approximately 5%) without tides than when tides are included, so the T simulation shows a better fit to the observations than the NT case.

Amplitudes and phases of all 15 constituents, present in the model forcing, are determined by harmonic analysis of the model solution for a period of the model run exceeding 90 days, necessary to separate the different harmonics. We analyzed sea surface height elevations, 3-D water velocity field, ice velocity, ice concentration, ice thickness, and shear stresses on the ice-ocean interface for different seasons and years. Shear stresses at the ice-water interface generate tidal motions of ice with diurnal and semidiurnal components. Figures 4a–4d show maxima of tidal velocities (sum of amplitudes) of ice and surface ocean currents for the semidiurnal band (“D2” includes M2, S2, and N2 harmonics) and diurnal band (“D1”: K1, O1, and S1), estimated for October–December 1979. For both the semidiurnal and diurnal tidal bands, the spatial pattern of the ice motion amplitude is similar to that of the surface current amplitude, the former is slightly weaker

Figure 2. Tidal amplitude and phase for (a) M2 and (b) K1 harmonics; critical latitudes for N2, M2, and S2 harmonics are shown in Figure 2a. (c) Scatterplot of model amplitudes of M₂ constitute versus Padman and Erofeeva [2004] assimilative model (gray points) and in situ observations (black crosses). (d) Relative maximum difference in M2 amplitudes between seasons: winter (JFMA), summer (JJAS), and autumn-winter (OND) for 2007, defined as a maximal difference over seasons, divided by seasonal mean amplitude of tide; (e) the same as Figure 2d but for 1979; and (f) relative difference for winter month between 1979 and 2007. The areas with amplitudes less than 0.01 m are excluded.

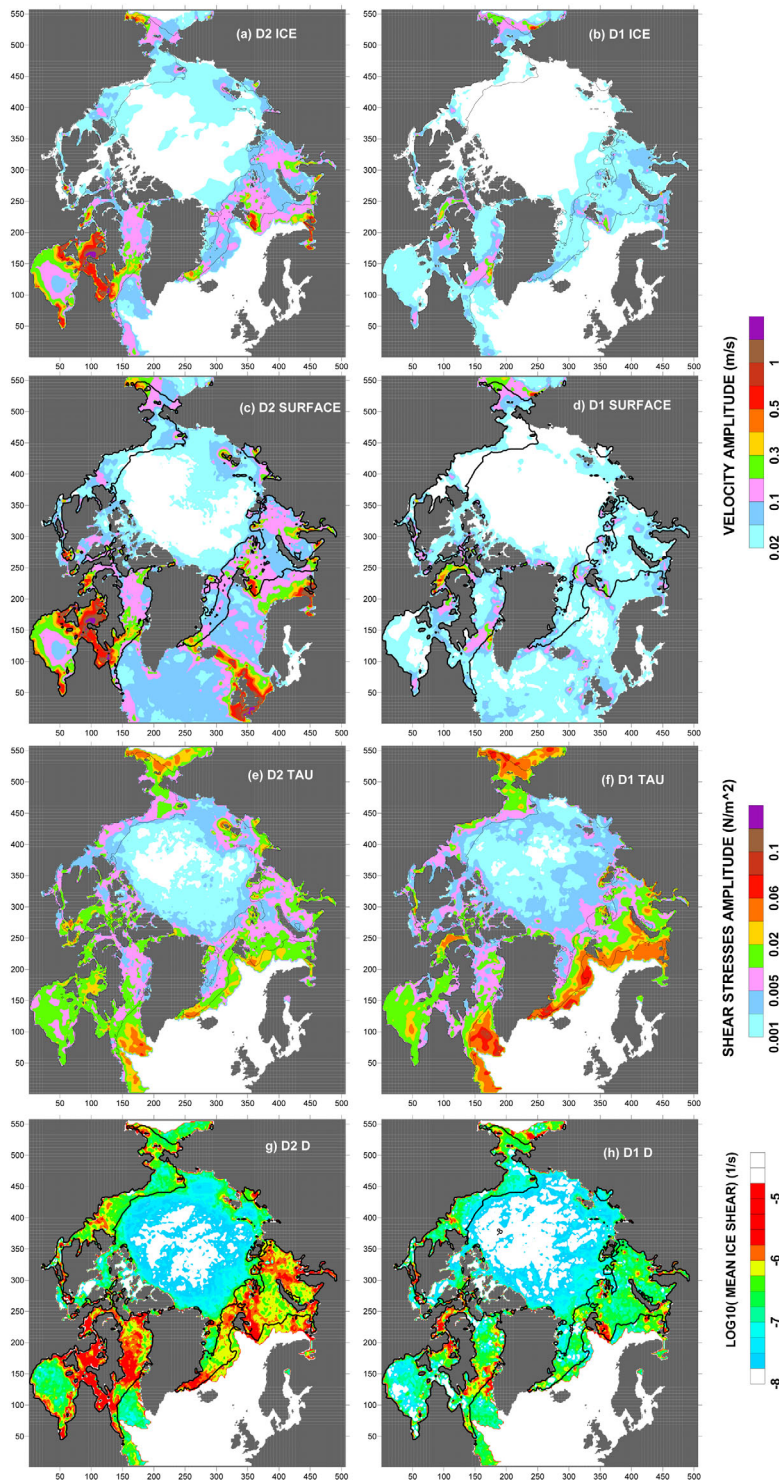


Figure 4. (a, b) Sum of tidal velocity amplitudes; (c, d) the same as Figures 4a and 4b but in the water surface layer; (e, f) corresponding shear stresses in the water under the ice; and (g, h) estimates of mean ice shear from ice strain rate and shearing stress, as given in Appendix A. “D1” denotes diurnal band of harmonics ($K1 + O1 + S1$) and “D2” semidiurnal band ($M2 + S2 + N2$), black contours designate the amplitudes of ice concentration of 0.01 for each band correspondingly.

than the latter (Figures 4a–4d). The diurnal components of tidal velocity are much weaker than those of the semidiurnal components; however, the amplitudes of the vertical shear stress at the ice-ocean interface (Figures 4e and 4f) are of the same order of magnitude, with a dominance of diurnal shear stresses in the deep ocean toward the pole and at the ice-edge. This can be explained by the presence of diurnal

variability in atmospheric forcing in autumn winter, contributing to an enhanced diurnal signal in the shear stress (the “meteorological” component of S_1). *Ray and Egbert* [2004], in examining altimetry data, found a “surprisingly large S_1 amplitudes in the North Pacific, the Okhotsk Sea and especially the Labrador Sea.” The region with ice concentration amplitudes (sum of amplitudes of D1 and D2 bands) exceeding 0.01, located between the Pole and open water, to large extent coincides with the area of seasonal ice for this year. In the model, we find tidal ice motions in the area of multiyear ice with velocity amplitudes exceeding 0.1 m s^{-1} off the northeast Greenland coast and still above 0.02 m s^{-1} near the Pole. This results in the sea ice lateral mean shear (a measure of mean deformation rates and shearing strain, see Appendix A) being 10^{-7} to 10^{-6} s^{-1} (Figures 4g and 4h), which is in agreement with estimates from the barotropic model of *Kowalik and Proshutinsky* [1994]. Using the sea ice differential motion derived from RADARSAT, *Kwok et al.* [2003] estimated similar deformation rates for the semidiurnal sea ice oscillations, although they argued that these could be due to the near-inertial oscillations of sea ice, rather than forced by tides. Harmonic analysis of individual frequencies (as conducted here for tides) is not appropriate for identifying near-inertial effects over a wide range of latitudes, so we cannot comment further on their role in this context; however, they can contribute to the D2 band near the critical latitudes. In the area of seasonal ice, diurnal currents produce oscillations in sea ice concentration and thickness at least twice as strong (with exception of Hudson Bay) as those produced by the semidiurnal tide (Figures 5a–5c). Oscillations of ice concentrations are negligible in the area of multiyear ice. Tidal motions do, however, affect sea ice thickness (i.e., mean thickness of the ice-covered fraction of the cell) in the areas of multiyear ice (Figures 5b and 5d). D1 generates areas of large oscillations in the ice thickness in the multiyear ice zone reaching 0.05–0.10 m in the northern edge of Greenland and 0.03m near the Pole (Figure 5d), exceeding the velocity amplitudes of the semidiurnal band (Figures 5b and 5d). The stronger effects of the diurnal tide can be explained by the D1 period being twice as long as for D2, leading to doubled transport time scales of ice during a half-tidal period.

4.2. Tidal Vertical Shear and Boundary Layers

Following *Prandle* [1982] and *Soulsby* [1983], we decompose tidal amplitudes onto clockwise (CW) R^- and counter clockwise (CCW) R^+ components of currents and calculate amplitudes and phases of vertical shear for both components [see also *Souza and Simpson*, 1996] from vertical profiles of amplitudes and phases of tidal velocity constituents. In agreement with theory for this latitude, vertical shear produced by the CCW component of currents (not shown) is concentrated in a very narrow layer near the bottom and is negligible compared with that of the CW component in the interior water column. Figure 6 shows maximum of amplitudes of tidal shear over the water column for the two most energetic CW components (M2 and S2) for October–December 1979. The maximum shear throughout the water column (Figure 6b) occurs at the surface (Figure 6a) for only a small region in the Kara and Laptev Seas. Tidal shear induced by M2 largely dominates. However, in some regions, S2 provides an equal contribution to the shear (Figure 6c). The level of shear estimated in the Laptev Sea [10^{-2} to $5 \times 10^{-2} \text{ s}^{-1}$] corresponds closely to observations [*Lenn et al.*, 2011; *Dmitrenko et al.*, 2012], with a strong spring-neap modulation [*Dmitrenko et al.*, 2012] due to S2–M2 interaction.

The strongest shear is generated along the entire Siberia coast, on the Yermak Plateau and the Storfjord Channel, the northern border of the Barents Sea (Figures 6b and 6c). Enhanced mixing in the Yermak Plateau is in an agreement with *Padman and Dillon* [1991] and *Fer et al.* [2010], the former observed internal waves of diurnal and quarter-diurnal amplitude, and the latter semidiurnal internal tides modifying AW inflow. Figure 6 (right) shows the turbocline depth (TD; this is the depth of the actively mixing layer, defined as the depth where turbulent diffusivity is larger than a threshold value of $1 \times 10^{-3} \text{ m}^2 \text{ s}^{-1}$; Figure 6d) and the depth of maximum shear (DMS; Figures 6e and 6f) for M2 and S2 tides. In the Laptev Sea (region A, Figures 6d–6f), the DMS is located below the TD, in agreement with observations by *Lenn et al.* [2011] and *Janout and Lenn* [2014]. In the Bering Strait, in the Chukchi Sea and above the Alaskan shelf of the Beaufort Sea, the DMS is also located below the TD (region B, Figures 6d–6f). In the vicinity of Fram Strait in the Nansen Basin, and also in the Greenland Sea and in the north-western Barents Sea (region C, Figures 6d–6f), as well as in the Canadian Arctic Archipelago, Baffin Bay, and Labrador Sea (region D, Figures 6d–6f), there is a strong similarity between TD and DMS, suggesting the existence of strong tidally generated mixing at the base of or below the mixed layer. Most of the strong shear production regions are located between the M2 and S2 critical latitudes.

To consider the vertical structure of the tide currents and shear in more detail, Figure 7 shows the amplitudes of the M2 component and RMS shear amplitude for two transects A and B (locations shown in Figure 6b). In

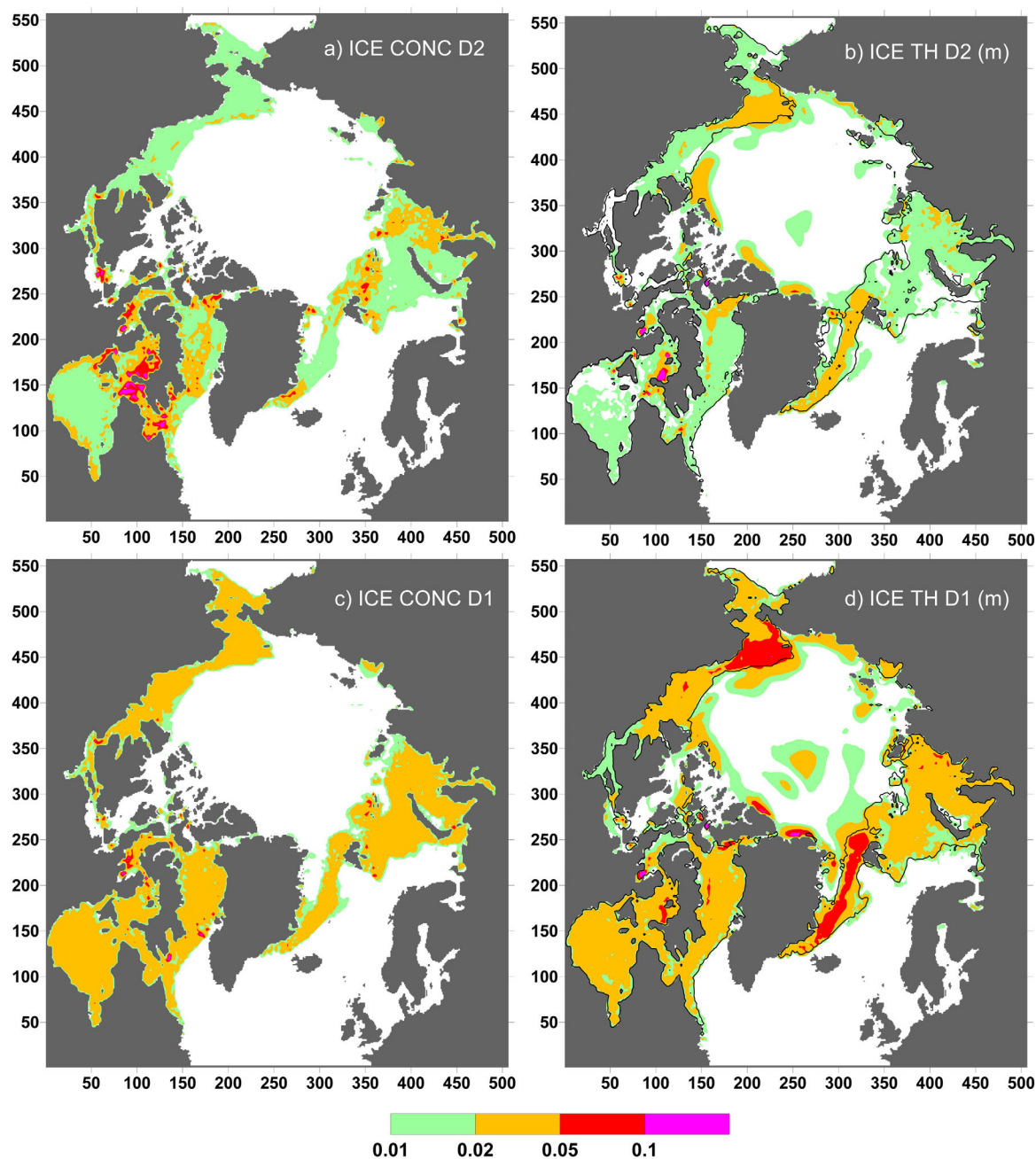


Figure 5. (a) The sum of semidiurnal amplitudes of ice concentration of D2 band ($M2 + S2 + N2$); (b) the same for ice thickness; and (c, d) the same as Figures 5a and 5b but for the diurnal D1 band ($K1 + O1 + S1$); black contours designate the amplitudes of ice concentration of 0.01 for each band correspondingly.

both transects, variations of amplitude strongly correlate with steepness of the bottom topography, with the larger amplitudes being present above the steep topography and also in shallower regions. The CW amplitude is strongly depth dependent, with multiple (surface and bottom) boundary layers and a strong subsurface shear at the base of the mixed layer and above rough bottom topography as seamounts and ridges.

The profiles of M2 and S2 CW current amplitude at locations X, Y, and Z are shown in Figure 8. Point X is located over a seamount in an area with little of ice cover and a relatively strongly mixed water column. At point Y, the ice concentration ranges from 0.2 to 0.7 during the analysis period (moving ice). In contrast, point Z is in a region of high sea ice concentration (>0.95) and slow moving ice. Point Y is characterized by relatively weak tidal currents but very strong subsurface shear amplitude reaching $2 \times 10^{-2} \text{ s}^{-1}$. In all

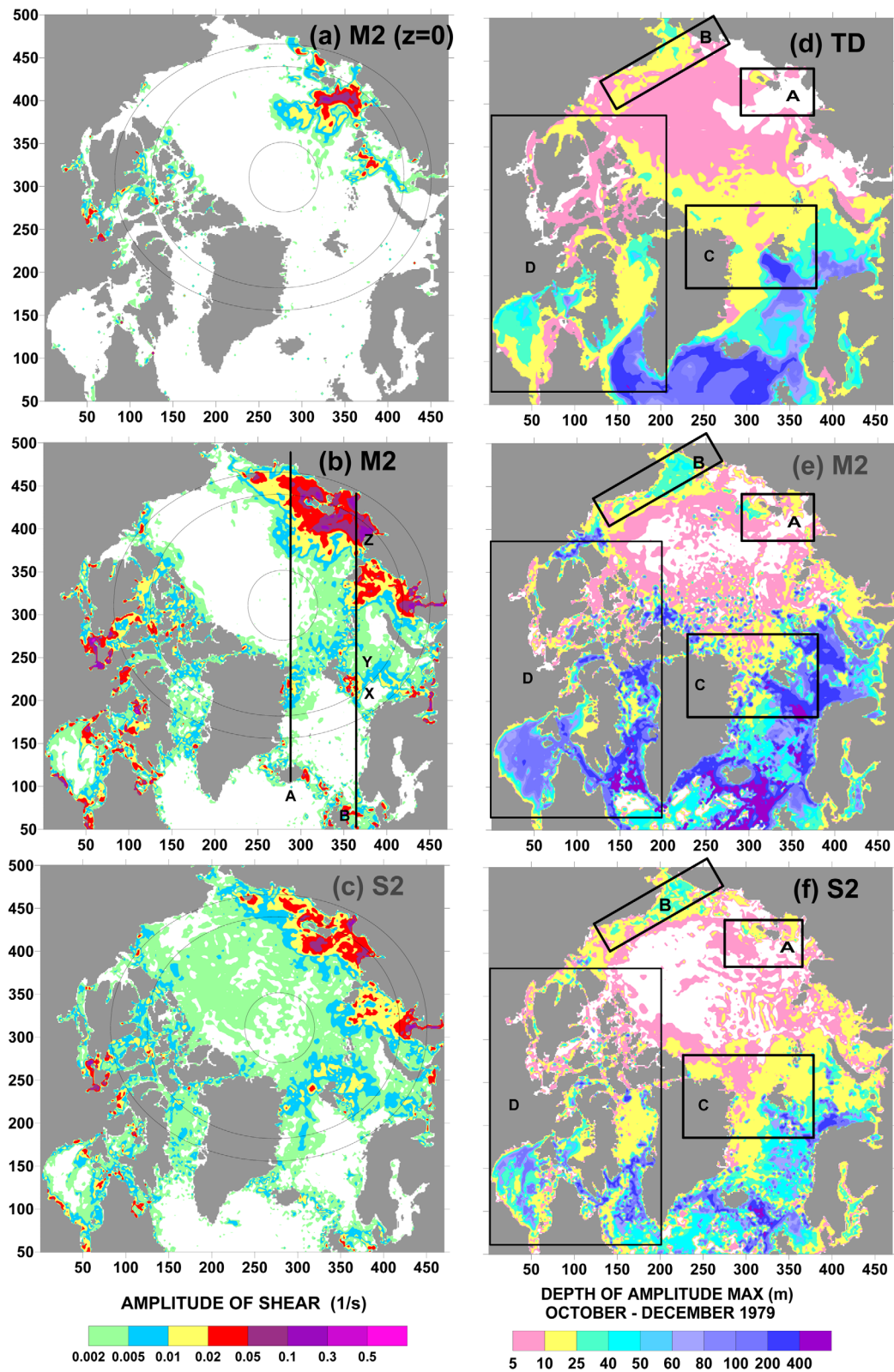


Figure 6. (a) Surface amplitude of shear for clockwise component of velocity for M₂ tides calculated by harmonic analysis of OND 1979 (color, white shows values below $2 \times 10^{-3} \text{ m s}^{-1}$), contours designate critical latitudes for N₂, M₂, and S₂ from south to the north; (b) the same as Figure 6a but for maximum shear over the water column; (c) the same as Figure 6b but for S₂-harmonic; (d) turbocline depth in meters (color, white shows depth less than 5 m) in December 1979, (e) depth in meters (color, white shows depth less than 5 m) where shear of M₂-amplitude reaches their maximum (i.e., depth of maximal shear, DMS); (f) the same as Figure 6e but for S₂. Rectangles (A–D) depict regions used for the analysis, details are in the text.

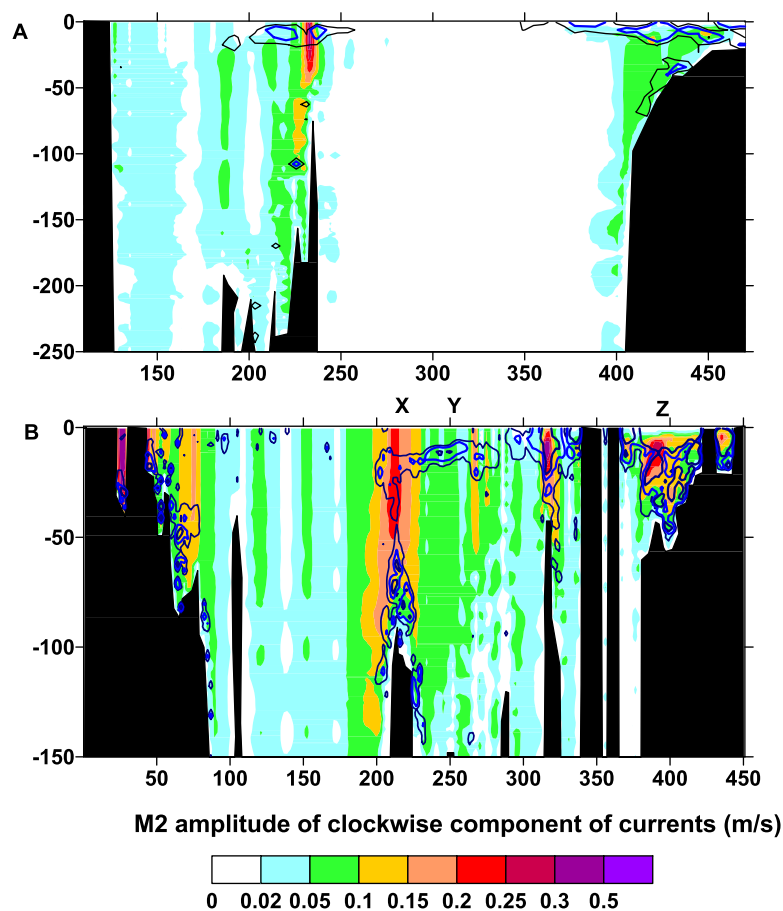


Figure 7. Amplitude of CW component of M2 velocity in transects shown in Figure 6b. Contours show sum of shear of all CW components: thin black line, 0.005 s^{-1} ; blue bold, 0.01 s^{-1} ; and black bold, 0.03 s^{-1} .

locations (Figure 8, left), the CW component of current is dominant and strongly depth dependent. At point X, the amplitude of the M2 component gradually grows with distance from the bottom and is nearly homogeneous in the upper 20 m. This results in negligible shear in the surface layer and nearly constant shear at intermediate (20–60 m) depths. The phase changes abruptly at the bottom boundary layer by $\sim\pi/2$ (at different depths for M2 and S2) resulting in a double-peak in shear near the bottom.

At point Y, in contrast, there is an evident structure and shift of amplitudes in the subsurface layer at ~ 20 m depth. This surface boundary layer is formed due to an interaction with the moving ice. Abrupt jumps in tidal current amplitudes and corresponding peaks in shear are important features observed and modeled in the pycnocline [Maas and van Haren, 1987; Souza and Simpson, 1996]. Much weaker and smoother variations in amplitude and phase are present at the top of the bottom boundary layer, resulting in a smaller peak in shear.

Point Z is located in the Laptev Sea, with ice concentration close to 1. All amplitudes decay toward the surface and bottom and are strongly depth dependent with maxima located at 10 m (similar to Dmitrenko et al. [2012, Figure 7] and Janout and Lenn [2014, Figure 8]). These profiles are typical for ice-covered areas in a strongly stratified water column [see e.g., Furevik and Foldvik, 1996; Makinson et al., 2006].

4.3. Residual Tidal Currents and Corresponding Vertical Motions

Residual tidal currents tend to be small-scale regional features concentrated over bottom topographic anomalies, with length scales similar to that of the topographic anomaly itself. However, these features can produce intensive quasi-steady vertical motions and in this case push warm Atlantic Water toward boundary layers and affect the mixing of water masses. A description of quasi-steady vertical velocity production terms is given in Appendix B. These terms include the tidal Reynolds stresses production terms (vorticity

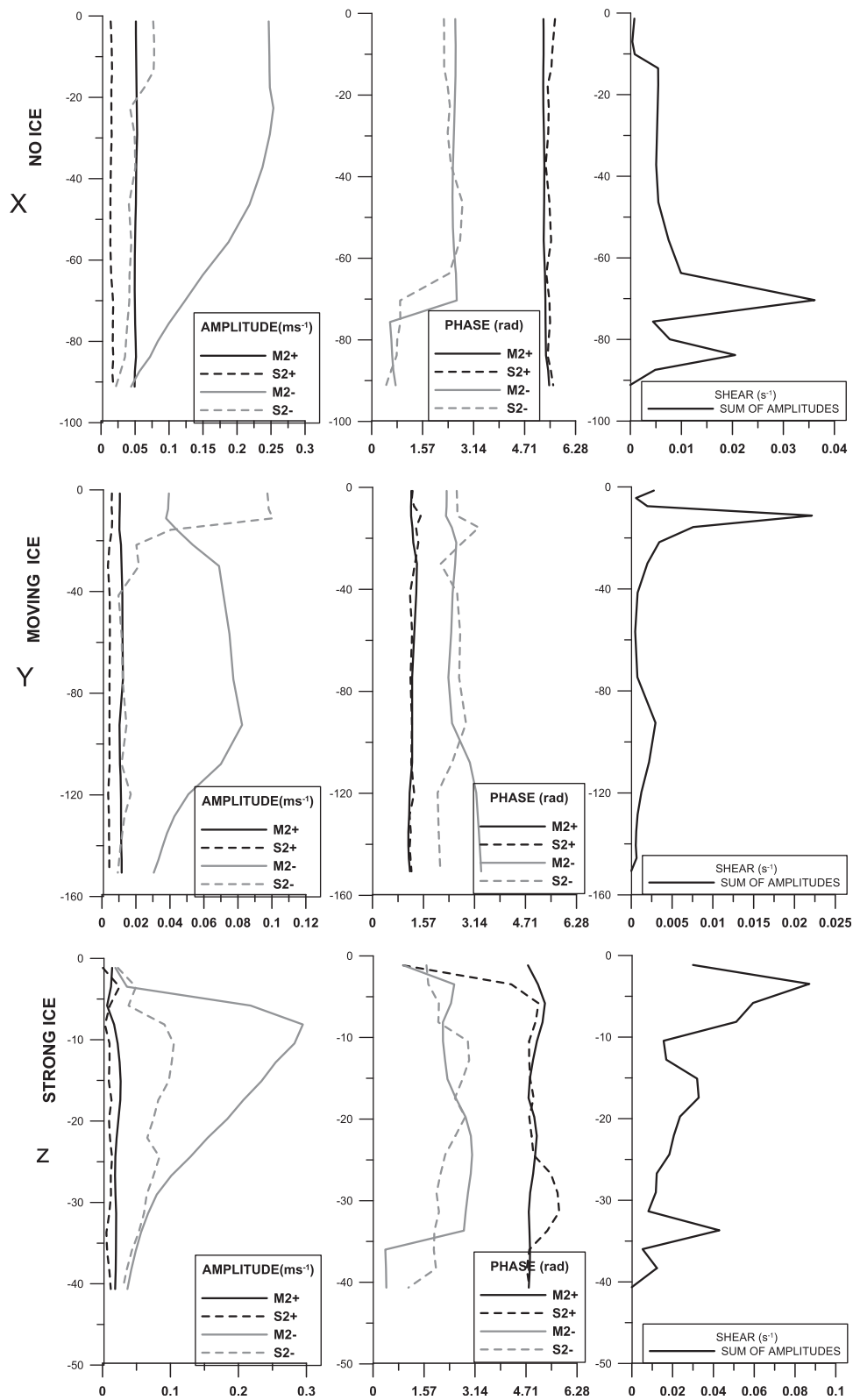


Figure 8. (left and middle) Depth profiles (m from surface) of CW(R^-) and CCW(R^+) components of amplitude and phase of M2 and S2 velocity at the locations X, Y, and Z shown in Figures 6b and 7b. (right) Sum of shear amplitudes for these two constituents. Point X is located in ice-free zone, point Y is located below moving ice with weak concentration (0.2–0.7), and point Z is located in the area of high ice concentration (>0.95).

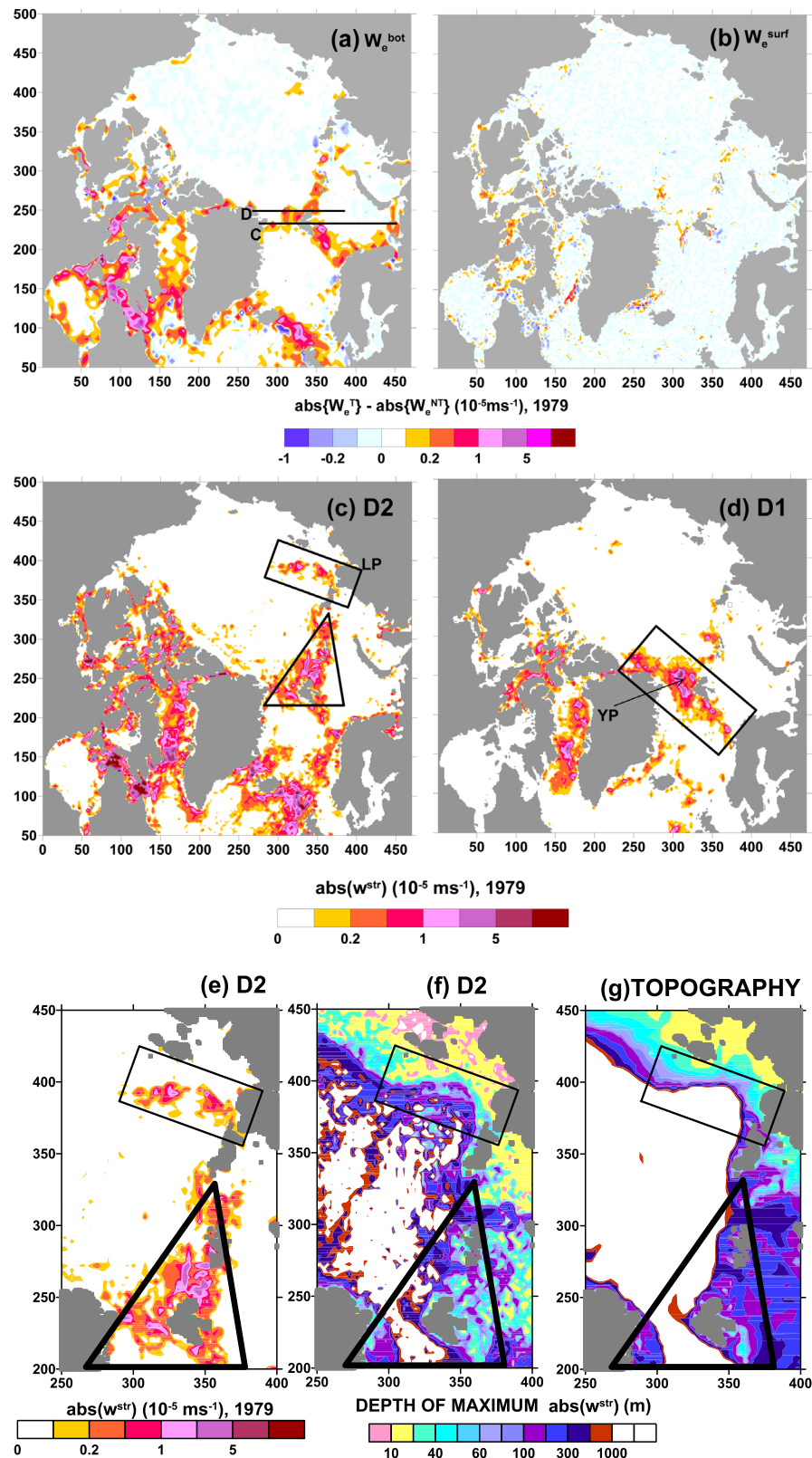


Figure 9. (a, b) Bottom and surface vertical Ekman pumping, estimated as difference between T and NT simulations, lines C and D designate the locations of transects, shown in Figures 12 and 13; (c, d) estimate of maximal vertical velocity due to tidal stretching of relative vorticity, given by equation (2) for semidiurnal and diurnal components of tides. YP denotes location of Yermak Plateau; LP, the Laptev Sea; (e) zoomed Figure 9c; (f) is the depth where Figure 9e reaches its maximum in magnitude; and (g) is the depth of the ocean for the same region as in Figures 9e and 9f.

stretching, tilting to vertical, and lateral advection of vorticity given by (B8)–(B10)), and boundary layer effects, i.e., the surface and bottom Ekman pumping (see Appendix B for definitions):

$$w_e^{bot} = (\nabla_H \times \{\tau_{bot}\}) / (\rho f), \quad w_e^{surf} = -(\nabla_H \times \{\tau_{io}\}) / (\rho f), \quad (1)$$

where $\{\}$ designates averaging over the tidal period. Tidal bottom and ice-ocean shear stresses depend on both the mean and tidal components of currents, so it is not possible to estimate Ekman vertical velocity from tidal velocities alone. We therefore calculate the tide-induced vertical Ekman pumping as the difference between the absolute values for simulations with and without tides for monthly mean shear stresses, thus filtering the fluctuating part of shear stresses through the averaging. The regions of strongest bottom Ekman pumping (Figure 9a) correspond to the gateways of AW to the AO (Figure 1): Fram Strait, Barents Sea openings, and the shelf break in the northern part of the Barents and Kara Seas, between Spitsbergen and Severnaya Zemlya. Ekman pumping in the interior waters cannot produce overturning circulations and result in geostrophic upwelling-downwelling of isopycnals. Surface Ekman pumping (Figure 9b) generated near the ice-ocean interface is much weaker, except in very small patches (Figure 9b).

Calculation of a quasi-steady vertical velocity field induced by tides is a nontrivial task that requires the solution of an omega-type elliptic equation [e.g., *Sanz and Viúdez, 2005*] with an extension to include the effects of tides on the right-hand side and on the boundary conditions (1). Interior sources of vertical motions, due to nonlinear tidal advection, produce ageostrophic circulations, which potentially could change the water mass properties through mixing or restratification. The strength of the vertical velocity and its location can be estimated from the stretching term in vorticity equation as

$$w_t^{vstr} = \int_{-H}^z \{(\nabla_H \times \mathbf{u}) \partial_z w\} dz / f \approx \{\zeta_t w_t\} / f, \quad (2)$$

where $\zeta_t = (\nabla_H \times \mathbf{u}_t)$ is the relative vorticity of the tidal current, w_t is tidal vertical velocity, calculated by harmonic analysis for a period of at least 90 days for each constituent. See section B3 for the expression of w_t^{vstr} in terms of tidal velocity amplitudes and phases. Figures 9c and 9d show maxima of absolute magnitudes of w_t^{vstr} for diurnal and semidiurnal components separately and the depths where w_t^{vstr} reach its maximum value (Figure 9f). A strong diurnal component of w_t^{vstr} ($>5 \times 10^{-5} \text{ m s}^{-1}$) is detected along Yermak Plateau and to the north of Greenland. This can be explained by topographic enhancement, and resonance of the diurnal tides with topographically trapped waves, which have been both observed [*Padman et al., 1992*] and simulated [*Kowalik and Proshutinsky, 1995*] at these locations. Both diurnal and semidiurnal components are strong along the Barents Sea openings and the Kara and Barents Seas shelf breaks. A strong semidiurnal component of quasi-steady vertical velocity is also detected at the shelf break of the Laptev Sea, with the depth of the maxima located far above the seabed (Figures 9e–9g), between depths of 50 and 200 m, in water depths greater than 1000 m (the regions are marked by a triangle and rectangle in Figures 9c and 9e). On the Barents Sea shelf, close to shelf break, the sources of w_t^{vstr} are located relatively close to the surface (10–25 m), which can potentially enhance the exchange between the fresh surface shelf waters and cold saltier water, formed during deep convection in the Barents Sea [*Schauer et al., 2002; Aksenov et al., 2010, 2011; Dmitrenko et al., 2014*]. The potential sources of tidally generated persistent vertical motions are also strong in Baffin Bay and the Canadian Archipelago.

5. Effects of Tides on the Arctic Upper Ocean and Ice on Seasonal to Annual Time Scales

To examine the integrated effects of tides on ice and ocean on the seasonal to annual time scales, we analyze year long runs with and without tides in 1979. We spin-up the model over 1978 with tides for both runs; then, in one of the runs, tides are turned off and dissipate over a day-month time scale, for simplicity we again use “T” and “NT” to identify these runs. Figure 10 shows the differences in properties between T and NT integrated over the AO under ice cover, where the concentration of ice is larger than 0.1. There are no significant changes in ice volume during the T and NT runs until April (Figure 10a). It is only then that the difference starts to grow, reaching around 6% in September and December, with a 2–5 cm reduction in the mean ice thickness. There are also changes in the turbocline depth (Figure 10b) at the start of winter, but these only become prominent during the next cold period, November–December 1979 (5% of total; mean depth difference of 1 m).

The difference in the total nonsolar heat flux from the water and in the heat flux from ocean to ice is negligible, except in December 1979 (Figure 10c). Hence, we conclude an increase in heat flux from the ocean to

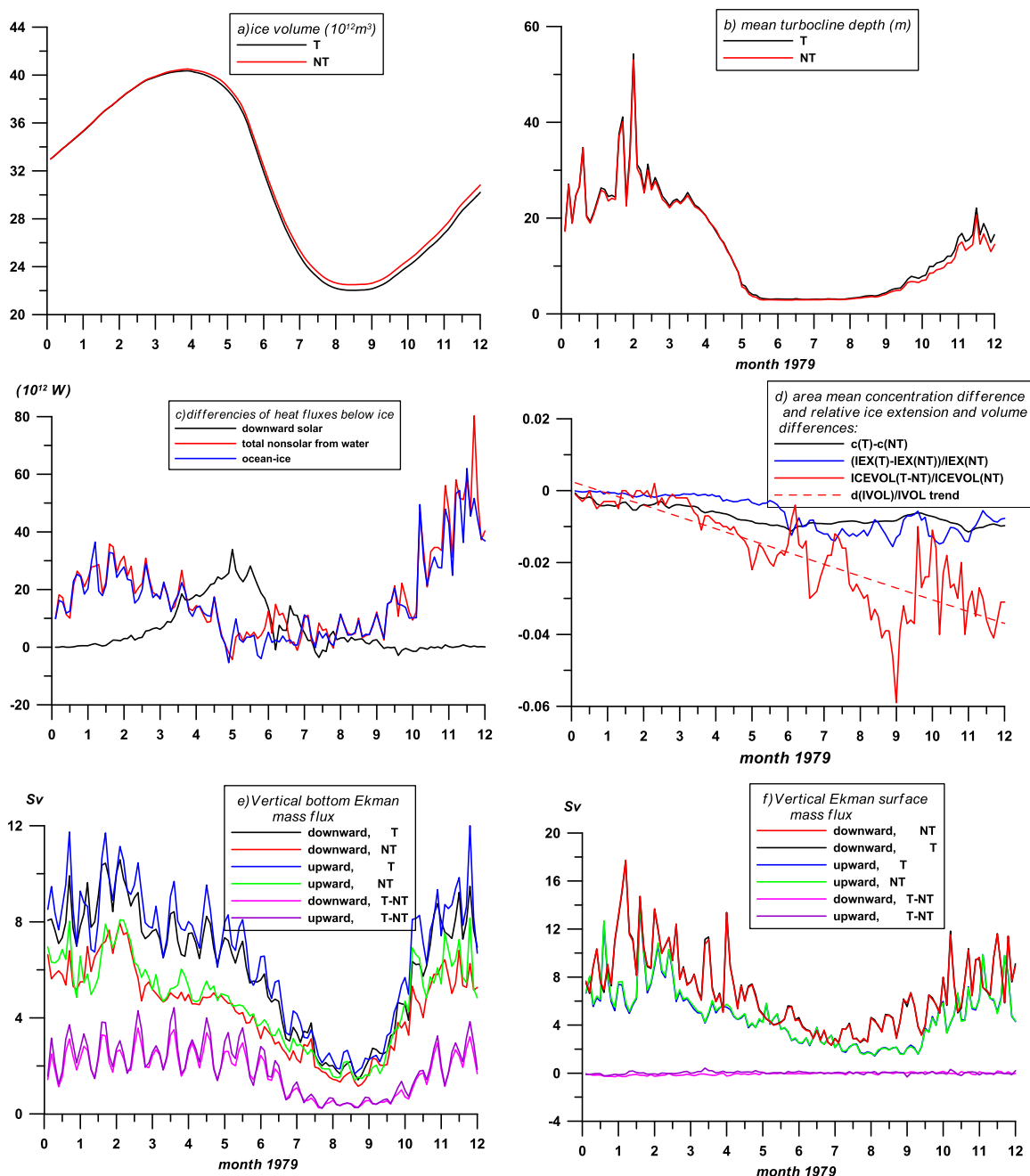


Figure 10. (a) Ice volume with time for T and NT simulations; (b) mean turbocline depth below the ice cover; (c) differences in heat fluxes between T and NT integrated below the ice cover: solar radiation, ocean to ice (OI) heat flux, and upward total nonradiative heat flux to ocean; (d) relative changes in the mean concentration, ice extent, and ice volume between T and NT simulations under the ice cover; (e) downward and upward cumulative vertical Ekman bottom mass fluxes under the ice cover and difference between T and NT cases; and (f) the same for the surface boundary layer.

atmosphere due to opening/closing of polynyas and leads is relatively small in this model. This is not surprising given that the model's comparatively coarse resolution does not resolve polynyas. However, the ice model is capable of generating grid-scale tidal variations in ice concentration (see section 4.1), thus, some effects of leads/polynyas are present in the model. In wintertime, the heat flux from the ocean to ice (OI) increases in the T run by ~5% in January–March ($+20\text{--}30 \times 10^{12} \text{W}$ compared with $400\text{--}600 \times 10^{12} \text{W}$ in total) and 10–12% in November–December ($+50 \times 10^{12} \text{W}$ compared with $400\text{--}600 \times 10^{12} \text{W}$ in total) (Figure 10c). In summer, the incoming solar radiation gained by the water increases by up to 5% in run T with a peak in May (Figure 10c). This leads to a small decrease in ice extent by 1% in June (Figure 10d) and mean

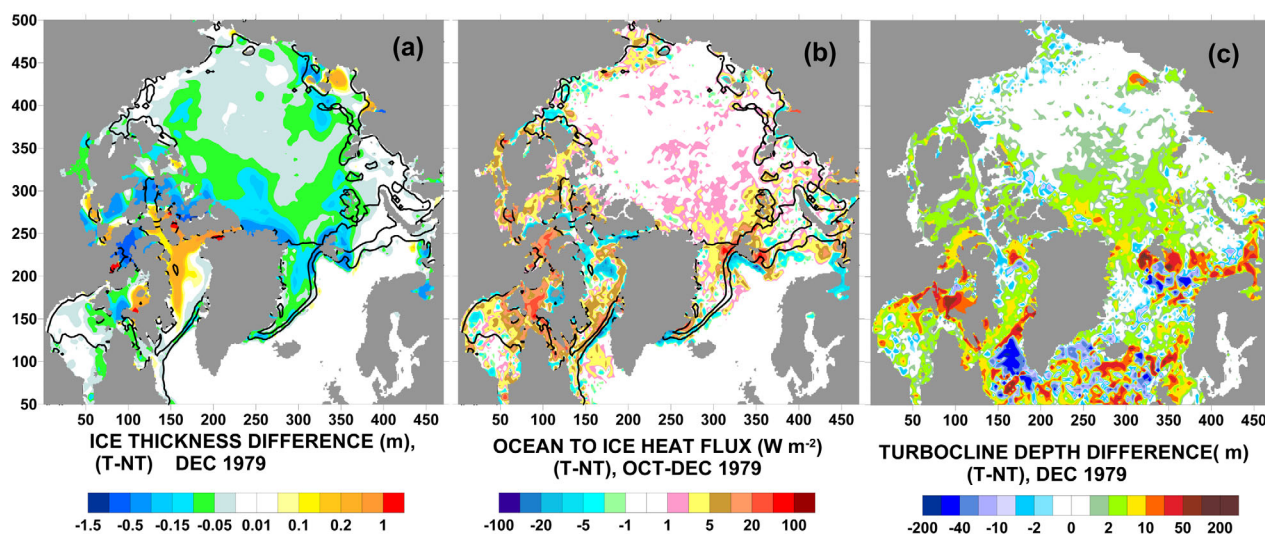


Figure 11. (a) Ice thickness difference in T and NT simulations after a year of simulations in December 1979; (b) ocean to ice heat flux difference OND 1979; and (c) turbocline depth difference, December 1979. Contours show ice concentrations (0.15, 0.75, and 0.9).

ice concentration by 0.01 (Figure 10d). A much larger decrease in ice volume is also seen, by up to 3% in July–September, with a peak of 6% in September, and a general trend of 3.9%/year. The former is explained by a secondary peak in the heat flux from the ocean during July in run T, following a peak in the difference in solar radiation flux between T and NT simulations in spring to early summer (Figure 10c). As a consequence, an opening and closing of ice takes place, resulting in an increase in the fraction of open water in summer and a decrease in the albedo in the T simulation. These effects have been discussed by *Koentopp et al.* [2005] in their modeling study of the Weddell Sea, where they found that a “combination of lower ice concentration, i.e., mainly enhanced absorption of radiation, and additional entrainment of warmer waters into the mixed layer by tidal currents, are responsible for an accelerated melting process in spring and a retarded expansion of the ice cover in early fall.”

In section 4.3, we discussed the sources of persistent quasi-steady motions induced by tides through surface and bottom Ekman pumping in the base of the boundary layers and internal sources due to nonlinear stretching of tidal vorticity over bottom topographic anomalies. To estimate the net role of quasi-steady vertical motions, produced by tides, we calculate net upward and downward bottom Ekman mass fluxes separately, following equation (1). Figure 10e shows the integral near-bottom Ekman mass fluxes for T and NT runs and their difference (under ice cover), using shear stresses averaged over 3 days. Upward and downward bottom mass fluxes are of the same order for each simulation, but with a net upwelling, and these exhibit strong seasonal and synoptic variability (the latter is evident from the NT run, green and red curves). The difference in the mass fluxes, due to tides, reaches 50% and is well correlated with the heat flux difference. Periodic oscillations in the mass fluxes of 14.04–14.6 days (roughly 25–26 oscillations per year) are also evident, which are absent in NT simulations. This period is close to $T = 2\pi / (|\omega_{S2} - \omega_{M2}|) = 14.35$ days, the period of low frequency M2–S2 interaction (i.e., the spring-neap tidal variation), as both constituents contribute to the bottom shear. There are no significant differences in the area average subsurface Ekman mass fluxes in T and NT simulations (Figure 10f), but local differences may well be important (not shown here). At the base of the surface boundary layer, downwelling Ekman pumping under the ice dominates over upwelling by 2 Sv. This is consistent with the general anticyclonic atmospheric circulation over the AO [*Proshutinsky and Johnson, 1997*]. Conversely, the situation is reversed at depth, where bottom Ekman pumping exhibits a net upwelling of 0.6 Sv. The surface Ekman pumping is acting over the entire basin, since it relates to the atmospheric circulation, while bottom shear stresses are prominent only over the shelf and slope, where bottom currents are strongest. Thus, the upwelling generated by bottom shear stress over varying topographic relief is amplified by 40–50% by tides and results in the penetration of AW into the surface layer.

After a year of simulation, the effects of tides lead to a decline in ice thickness of ~ 0.05 to ~ 1 m almost everywhere, except Baffin Bay (Figure 11a) and corresponds to a much deeper turbocline depth (TD)

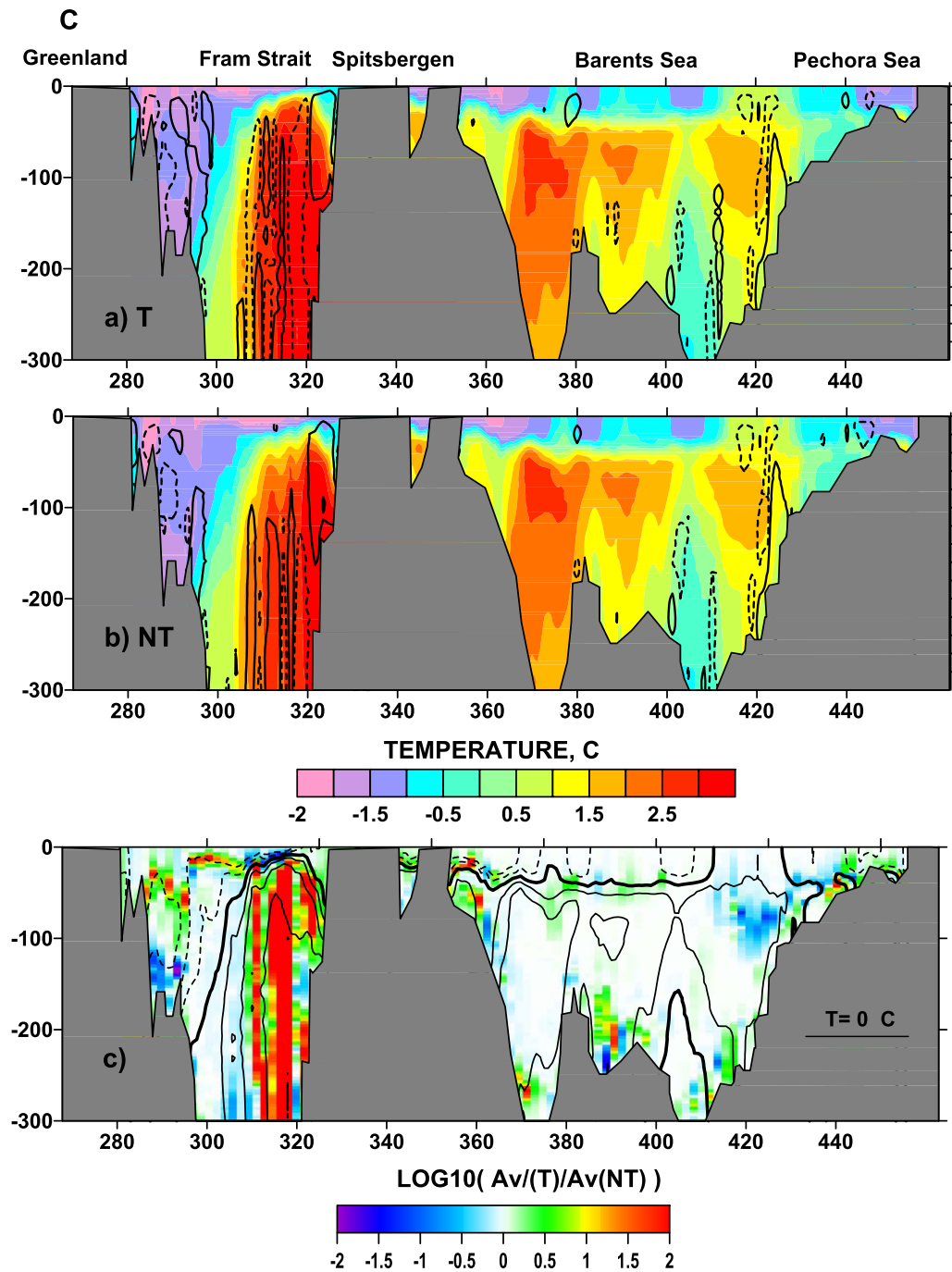


Figure 12. (a, b) Monthly mean temperature and vertical velocity for T and NT simulations for the transect C shown in Figure 9a; dashed line: $-1 \times 10^{-5} \text{ m s}^{-1}$ and solid line: $1 \times 10^{-5} \text{ m s}^{-1}$. (c) The ratio of monthly mean vertical diffusivities A_v , in T and NT simulations in logarithmic scale (December 1979). Contour shows temperature for T simulations and dashed lines denote negative values.

(Figure 11c). The strongest reduction in ice thickness is observed around Spitsbergen (Svalbard), north of Greenland, in the Laptev Sea, Foxe Basin, and Canadian Archipelago. These changes are well correlated with both the spatial pattern of OI heat flux increase and the decrease of turbocline depth (Figures 11b and 11c). The OI heat flux increases by 10–30 W/m^2 near the Yermak Plateau and Storfjord Channel; the former is in agreement with the observations of Padman and Dillon [1991] and Fer et al. [2010]. Comparing this with Figure 9a, we find that locations of intense vertical bottom Ekman pumping correspond to locations of increased OI heat flux and TD variation.

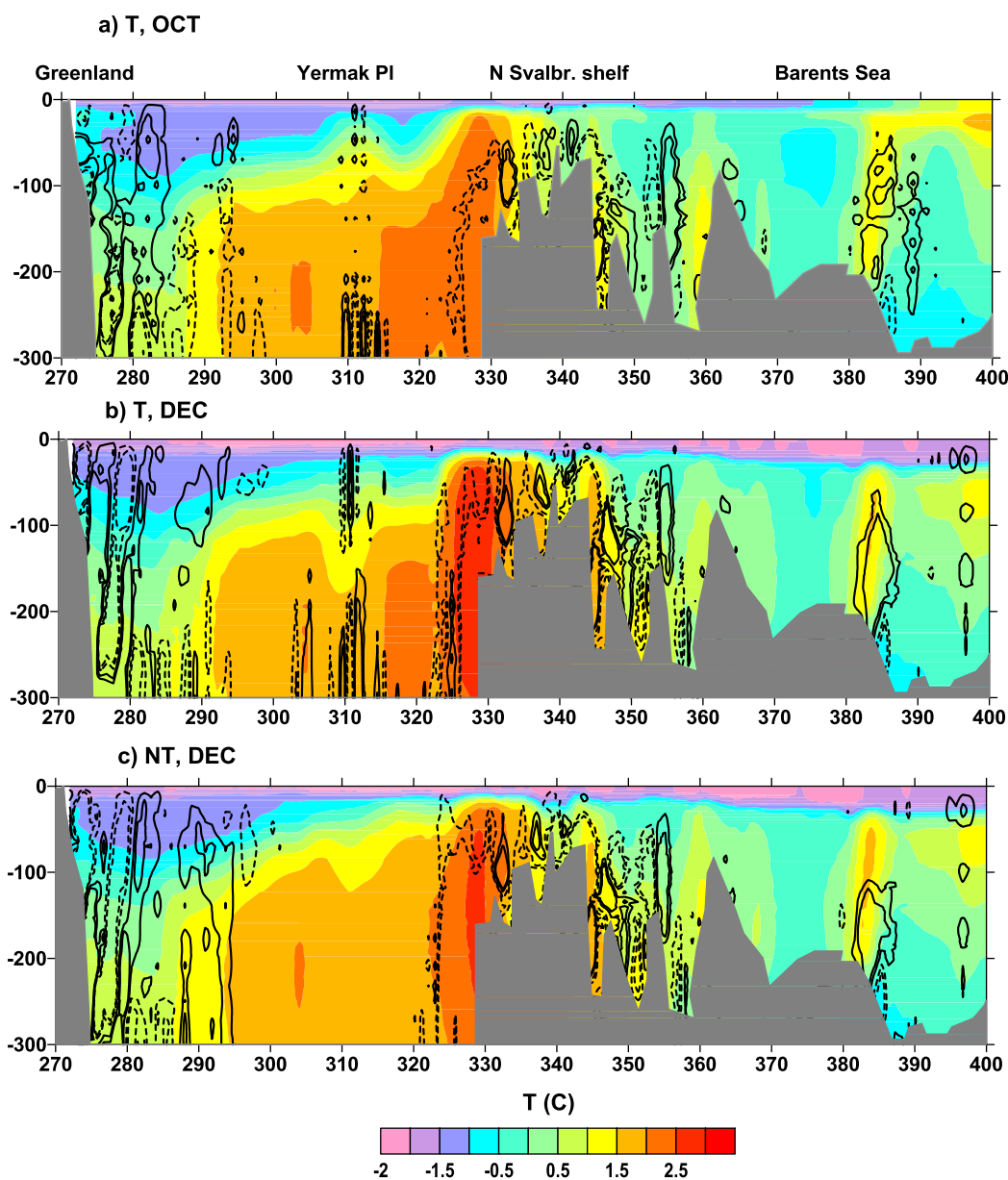


Figure 13. Monthly mean temperature and vertical velocity for the transect D shown in Figure 9a. (a, b) T simulations for October and December, (c) NT case, December (-1 ; -0.5 ; 0.5 ; 1) $\times 10^{-5}$ m s^{-1} . Vertical velocity contours are shown and dashed lines denote the negative values.

Tides intensify quasi-steady vertical motions and mixing in the Fram Strait which produce changes in the AW inflow properties (Figures 12a and 12b). Monthly mean (December 1979) temperature and quasi-steady vertical velocity on the transect C (shown in Figure 9a) are mostly the same in the Barents Sea, while across Fram Strait, there are intense vertical motions in both the warm core (off Spitsbergen coast) and the cold core (from Greenland side). The Atlantic core in the T run is much closer to the surface and intense vertical motions ($>10^{-5}$ m s^{-1}) penetrate to depths of 10–20 m from the surface. Figure 12 (bottom) demonstrates the increase of vertical diffusivities in T run versus NT case in the Atlantic layers by up to 2 orders and by 2–10 times in the most of pycnocline regions. This figure is a good illustration of the interaction between two mechanisms capable of transforming water masses: increased mixed layer depth due to tidal shear and thick Ekman depth (2.2) and vertical motions associated with tidally driven residual currents (2.4).

Transect D is located north of transect C (see Figure 9 for location) shows the effects of ice-ocean shear stresses on the formation of quasi-steady vertical motions and tidal coupling between the surface and bottom

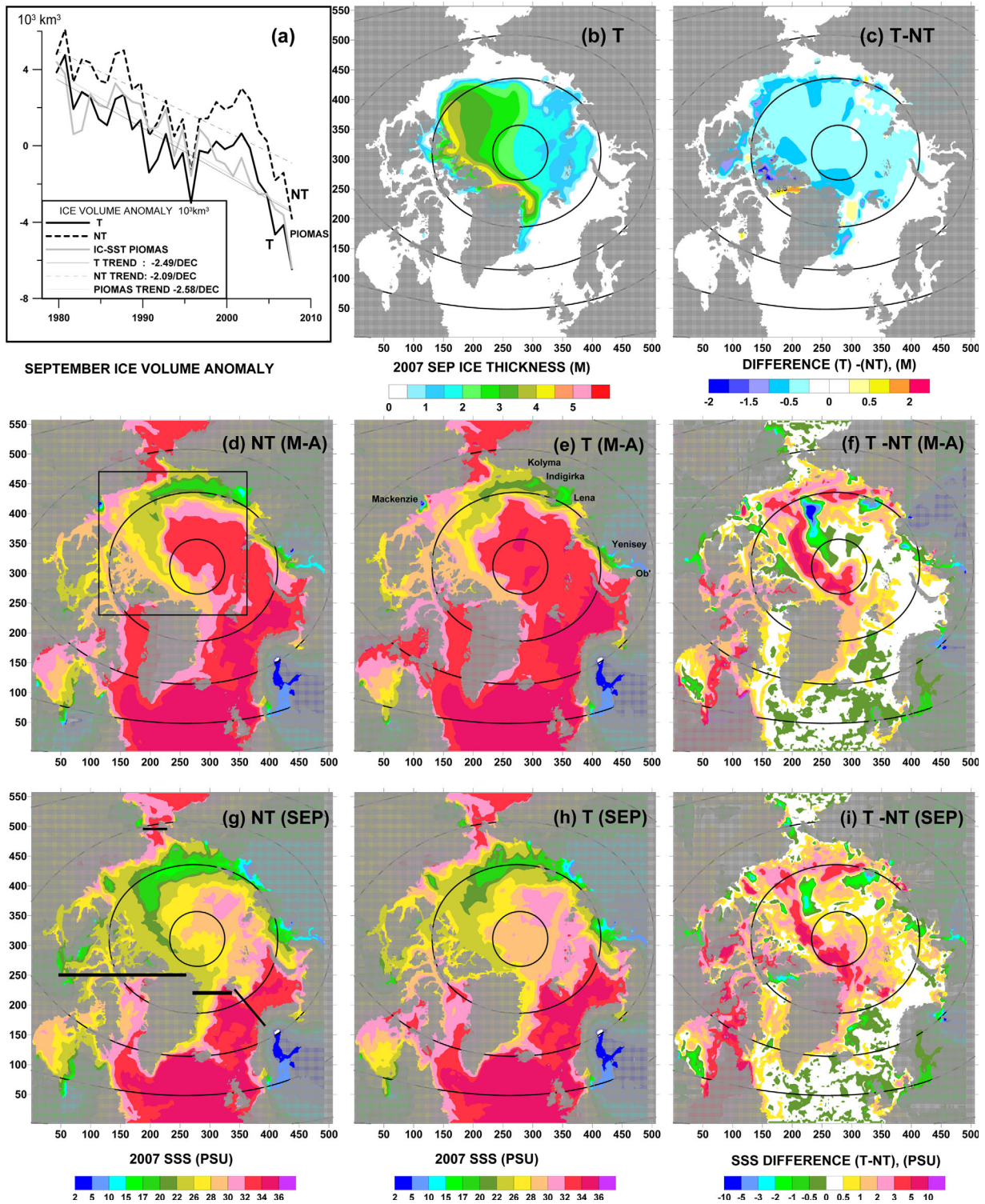


Figure 14. (a) Ice volume anomaly in September over 30 years of simulations for T and NT runs and IC-SST PIOMAS simulations; (b) ice volume in September 2007; (c) ice volume difference between T and NT simulations in September 2007; (d–f) SSS winter (March–April) 2007 for NT and T simulations and their difference (T) – (NT); and (g–i) the same as Figures 14d–14f but for September 2007; Figure 14d also shows domain for calculations of mean salinity and heat content, Figure 14g shows the region of fresh water content calculation as in *Jahn et al.* [2012], in Figure 14e location of main rivers are shown.

layers (Figure 13). The area of intense vertical motions is located above the north side of the Yermak Plateau and extends from the bottom (depth of 800–1000 m) upward to a depth of 200–300 m. The maximum vertical velocity reaches $1\text{--}2 \times 10^{-4} \text{ m s}^{-1}$ at a depth of 300–400 m (not shown here). These large vertical velocities can be formed by the vorticity stretching of the tidal currents (Figure 9d). In October (Figure 13a), ice just starts to form, and there is little vertical motion in the subsurface layer at this location. With ice forming during November and December, the appearance of vertical motions in the subsurface upper layer becomes evident (Figure 13b) and is collocated with intense vertical motions in the deeper layer, which are absent in NT simulations (Figure 13c). We attribute the formation of strong subsurface vertical motions in December to the appearance of the second solid boundary at the surface and hence the generation of vorticity by ice-ocean shear stresses. In December, we detect substantial changes in AW due to tidal effects.

6. Multiyear Effects of Tides on Ice and Ocean

The 1 year simulations with and without tides, discussed in section 5 demonstrate prominent changes due to tides. Here we consider the effects of tides integrated over three decades (1978–2007).

The 30 year T and NT simulations both show a negative trend in September sea ice volume (month of minimum ice volume, Figure 14a), but with a significantly stronger decrease in the T simulation: $\sim 2.49 \times 10^3 \text{ km}^3/\text{decade}$ compared with $2.09 \times 10^3 \text{ km}^3/\text{decade}$ in the NT simulations. During March (the month of maximum ice volume), over this period, the negative trend increases to $-2.54 \times 10^3 \text{ km}^3/\text{decade}$ in T case and decreases to $-2.05 \times 10^3 \text{ km}^3$ in NT simulations. In total, tides are responsible for about 15–17% of the modeled ice volume reduction (Figure 14a) by the end of 30 year simulations, with an average difference over this period of $\sim 11\%$. We have performed four additional simulations with different “ice strength” parameter, P^* , in the range: 1×10^4 to $2 \times 10^4 \text{ N m}^{-2}$. In all these simulations, the rate of ice volume reduction differs slightly, but with the same effect of the tides being apparent: tides accelerate the ice volume decrease by 12–17% over 30 years.

Schweiger *et al.* [2011] compared ice volume anomalies for three different PIOMAS simulations with different ice models: with assimilation of ice concentration and SST (IC-SST run), ice concentration assimilation only (IC), and without any assimilation (NA). Their model was run from 1958 to 2010, with a comparison period from 1979 to 2010. All these simulations showed good statistics for ice thickness compared with submarine-based sonar measurements. They found ice thickness trends to be -0.15 , -0.19 , and $-0.20 \text{ m decade}^{-1}$ in March and -0.25 , -0.33 , and $-0.37 \text{ m decade}^{-1}$ in October for IC-SST, IC, and NA runs, respectively. For ice volume anomaly, PIOMAS gives trends of $(-2.8, -3.5, \text{ and } -3.8) \times 10^3 \text{ km}^3/\text{decade}$, respectively, with estimated uncertainty to be $1 \times 10^3 \text{ km}^3/\text{decade}$. For March, our study predicts ice thickness trends -0.146 and $-0.124 \text{ m decade}^{-1}$ for T and NT simulations, respectively. The equivalent rates for October are -0.230 and $-0.194 \text{ m decade}^{-1}$. The T run is very close to the IC-SST estimate both for ice volume (-2.53×10^3 versus $-2.8 \times 10^3 \text{ km}^3/\text{decade}$) and thickness (-0.146 versus $-0.15 \text{ m decade}^{-1}$ in March and -0.230 versus $-0.25 \text{ m decade}^{-1}$ in October, respectively) and in the range of the uncertainty of the mean value ($-3.4 \times 10^3 \text{ km}^3/\text{decade}$) of the three PIOMAS runs. Thus, including tides in the model increases the downward trend in the sea ice volume and therefore improves the agreement with PIOMAS. However, PIOMAS trend takes into account the faster decline of ice during 2008–2010, whereas our model stops in 2007. Recalculating the IC-SST PIOMAS ice volume trend for the period of 1979–2007 in September, as shown in Figure 14a, demonstrates an even better agreement with T runs: IC-SST PIOMAS: $-2.58 \times 10^3 \text{ km}^3/\text{decade}$ versus T simulations: $-2.49 \times 10^3 \text{ km}^3/\text{decade}$ and NT simulations: $-2.09 \text{ km}^3/\text{decade}$. While our model here overestimates total ice volume compared with PIOMAS, it predicts the trends well. Thus, including tides reduces the error in ice volume and ice thickness trend from 20% (NT) to 4% (T). The $\sim 10\%$ excess ice volume is a common bias in this configuration with the LIM2 model [e.g., Popova *et al.*, 2013]. It is caused by using sea ice thermodynamics with a simplified sea ice thickness distribution function, which assumes that the ice thicknesses is uniformly distributed between zero thickness and twice the mean ice thickness value in the ice-covered part of model the grid cell [Fichefet and Maqueda, 1997]. The bias is not detrimental for the present analysis. Spatial differences between the T and NT runs in September (ice extent minimum) in 2007 (Figure 14c) show a decline of ice thickness of generally 20–50 cm and up to 1 m in the Canadian Archipelago.

Tides significantly change the surface salinity on multidecadal time scales; on average surface salinity at the end of the 30 year run is ~ 1 PSU higher across the whole model domain (including Atlantic and Bering Sea regions) in the tidal case and 1.8 PSU higher across the deep ($>500 \text{ m}$) part of the AO (see domain in Figure

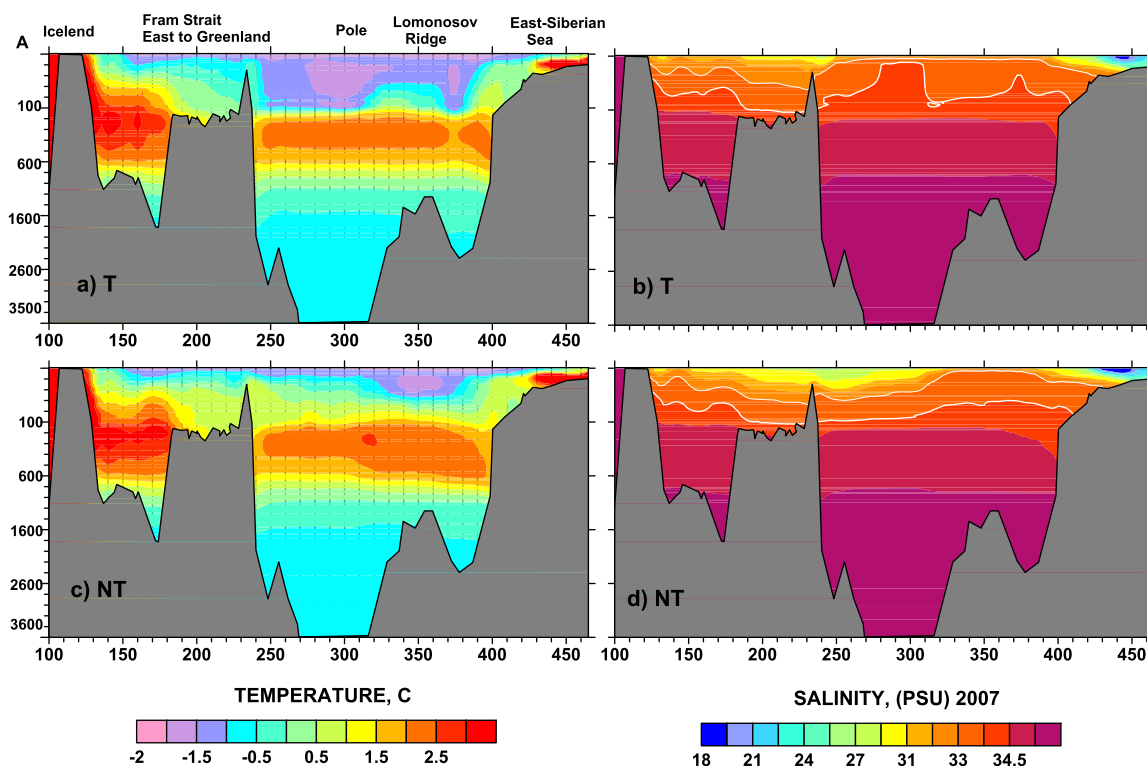


Figure 15. Yearly mean temperature and salinity along transect A shown in Figure 6b for simulations with and without tides.

14d) with anomalies reaching 8 PSU (Figure 14f). The surface salinity exhibits strong annual variability with the differences of about 2 PSU between winter (March–April, Figures 14d and 14e) and summer (September) (Figures 14g and 14h). In winter, the spatial mean difference between T and NT run reaches a maximum of 2 PSU, decreasing to 1.46 PSU in September and 1.3 PSU in January. A further decrease of surface salinity in the deeper part of the basin is as a lagged response to the signal from fresh river runoff. In both simulations, surface salinity decreases with time, but the rate of decrease is lower in the tidal case.

For both the T and NT simulations, we calculate the mean 1992–2001 total liquid freshwater content (FWC) in the upper 250 m of the Arctic Ocean for the area marked in Figure 14d. Hereafter, all the FWC calculations are referenced to the mean Arctic salinity of 34.8 PSU. In these runs, FWC is similar, being 69×10^3 and 70×10^3 km³, respectively, for T and NT, and is in a good agreement with the FWC of 74×10^3 km³, obtained by Jahn *et al.* [2012] from the University of Washington Polar Hydrography Center (PHC) climatology [Steele *et al.*, 2001]. Our results are also within the FWC range of 56×10^3 to 87×10^3 km³, simulated in the Arctic Ocean Model Inter-comparison Experiment (AOMIP) [Jahn *et al.*, 2012, Table 3]. Differences in the AOMIP models are due to differences in model physics and resolution [Jahn *et al.*, 2012]. Spatial distribution of the fresh water in our simulations is similar to the global ORCA25 AOMIP simulations and climatology [cf. Jahn *et al.*, 2012, Figure 2a]. Similar to most of the models in Jahn *et al.* [2012], T and NT runs show a high FWC in the Beaufort Sea, in agreement with observations in the 1990s from Proshutinsky *et al.* [2009] and Rabe *et al.* [2011]. The differences in spatial distributions of FWC between T and NT runs are much smaller than the spread in the AOMIP models.

In the upper layer (0–100 m), the freshwater content (calculated in the rectangle shown in Figure 14d) exhibits natural variability in phase with the atmospherically forced circulation [e.g., Proshutinsky and Johnson, 1997]. It is, however, lower in the T case than NT by 6–7% in 2007 (36.3×10^3 versus 42.26×10^3 km³ NT) partly at the expense of the intermediate layer of 100–500 m depth, which gains 1.81×10^3 km³ more freshwater in the T case (18.4×10^3 km³ in T versus 16.6×10^3 km³ in NT). Thus, a deficit of 1.06×10^3 km³ of freshwater in the upper 100 m in the tidal case can be explained by changes in shelf-deep ocean exchange or by exchange with the Atlantic Ocean. Indeed, in Figures 14d and 14g, we see a longer tongue

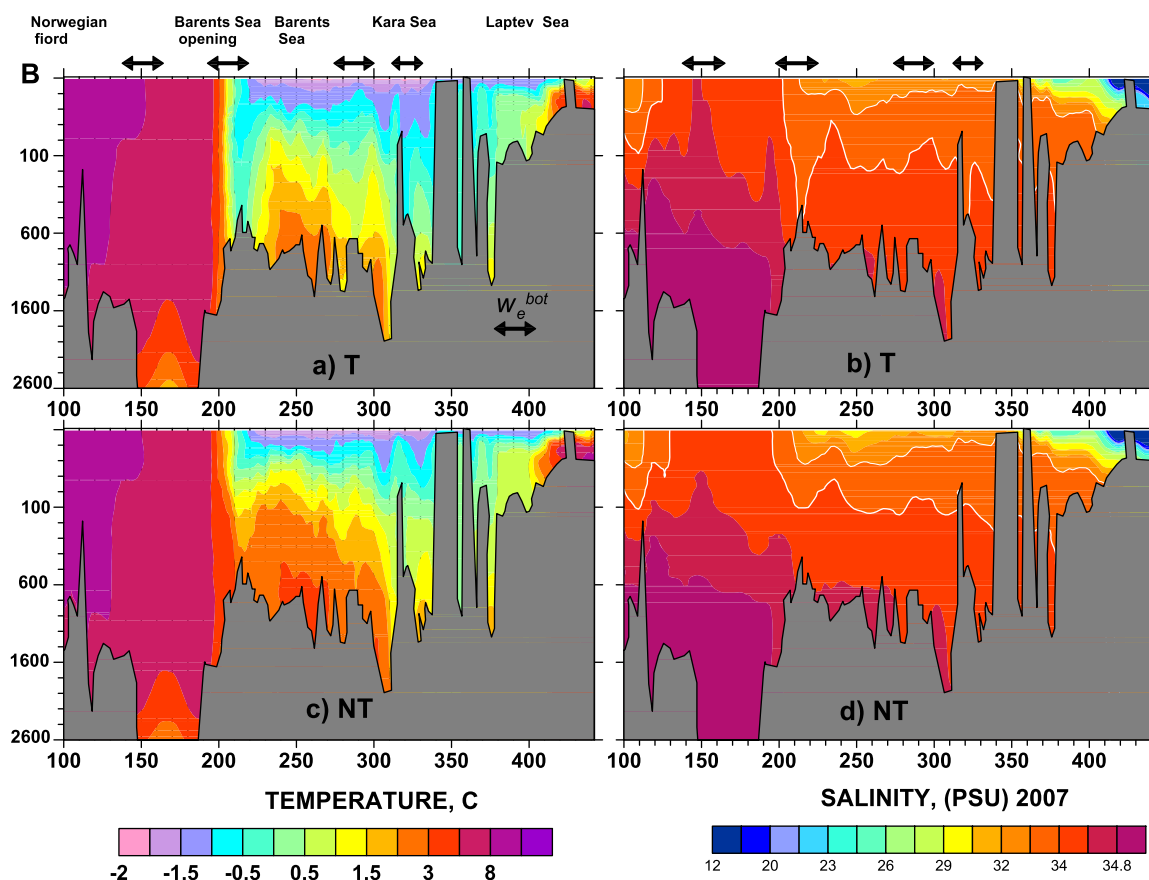


Figure 16. The same as Figure 15 but for transect B. Arrows mark the areas of strong vertical bottom pumping due to tides (see Figure 9a).

of freshwater outflowing along the East Greenland coast. The deep AW layer (500–1000 m) in the AO continuously freshens, but with a weaker trend in the tidal case ($1.29 \times 10^3 \text{ km}^3$ less freshwaters in T than NT over 30 years) with little change to the salinity in the deepest layer (1000–4000 m).

Adding tides also result in strong changes in the surface freshwater signal along the East Siberian coast (Figures 14d–14i). The surface freshwater signal from the Lena and Yenisey estuaries propagates counter clockwise with increased salinity along the coastline and shelf break, and a negative salinity anomaly in the outer part of the Canadian Basin. Tides result in the dilution of riverine freshwater with surrounding saltier waters, which changes stratification, baroclinic pressure gradients and modifies the surface circulation in AO. In the NT case, the fresh water signal penetrates much further to the south along the east Greenland coast in comparison with the tidal case (Figures 14d and 14e). The origin of the salinity anomaly signal is very well correlated with tidally increased shear in the intermediate layers, as shown in Figure 6.

As shown previously by *Holloway and Proshutinsky [2007]*, we also find that tidal effects slow down the strong warming trends in the central AO that are seen in many ocean models. However, we find a weaker effect in the current model than reported by *Holloway and Proshutinsky [2007]*. Surface to seabed depth integrated heat content trend (calculated in the rectangular box shown in Figure 14d relative to temperature 0°C) in our model is positive, reducing from $6.3 \times 10^{20} \text{ J/year}$ in NT case to $5.7 \times 10^{20} \text{ J/year}$ in T. In the upper 100 m, heat content (negative due to average negative temperature) grows in the upper 0–100 m layer from -0.3×10^{22} to $-0.05 \times 10^{22} \text{ J}$ in T case and from -0.3×10^{22} to $+0.062 \times 10^{22}$ in NT case with about a 30% difference in trends.

The strong changes in the water mass properties in the AO due to tidal effects can be seen in transects of yearly mean salinity and temperature in 2007 (Figure 15) for T and NT. Transect A (location shown in Figure 6b) crosses the entire AO near the Pole from the Greenland coast to the East Siberia Sea. Similar to the results of *Holloway and Proshutinsky [2007]*, which demonstrate a cooling of the AO in the comparison with nontidal

simulations, our model predicts a thinner AW layer and a much colder and saltier upper 100 m in run T compared with NT. Near the Pole, a colder saltier core forms in the upper 100 m in the T run (see also Figure 14e).

Figure 16 shows yearly mean temperature and salinity in the transect B (location marked in Figure 6b), which crosses the Eurasian shelf and the Barents/Kara Seas openings, intersecting three areas of potential tide-induced Ekman bottom vertical pumping (see Figure 9a, in Figure 16 these zones are marked by arrows). In general, AW in the AO is colder and shallower in T simulations than in NT. We find the T case is characterized by much sharper isotherms and isohalines with multiple outcroppings from the surface to the bottom at the locations of strong tidal vertical Ekman pumping. Outcroppings of isopycnals in the NT case also take place but are shallower and never reach the seabed.

These results are relevant to the results from section 5, where we find that tidal effects are particularly important on the ocean to ice heat fluxes, with a much smaller effect on the ocean-atmosphere exchange. Since ice melting is stronger in the tidal simulations, but the surface salinity is higher, we conclude that tidally induced mixing is a more important effect than ice formation due to the convergence-divergence of ice. This is not surprising given the comparatively coarse resolution of the model.

7. Conclusions

In this work, we have explored four hypotheses (A–D), formulated in the introduction (section 2.5). Hypothesis (A) considers the role of opening and closing of leads, produced by tidal convergence-divergence, on the heat exchange between ocean and atmosphere and ice production. Our model reproduces the tidal motions of ice, tidal stresses, and levels of ice concentration variability that are consistent with available observations (section 4.1). We have found that in this particular model (NEMO/LIM2) and with this particular resolution (10–15 km), the open and closing of leads affects heat exchange with the atmosphere: however, the sign of this flux differs between the summer and wintertime. In summer, this process reduces the net surface albedo, resulting in an increase in short-wave radiation flux to the ocean, while in winter, there is an increase in heat loss (long-wave, sensible, and latent heat fluxes) from ocean to atmosphere (see Figure 10). However, these changes in heat fluxes are secondary in comparison with the net increase in heat flux from ocean to ice, resulting in the acceleration of ice decline due to tides. We note that the magnitude of this effect will be subject to improvements in model resolution and in ice model physics (e.g., embedding of ice in the ocean, using a multicategory ice model, and including ice-ocean roughness drag variability).

Hypotheses (B) and (C) both consider the role of tidal shear at latitudes close to critical. In section 4.2, we demonstrate that, in accordance with the theory and observations, anticyclonic (clockwise) component of tidal current generates very thick boundary layers in a weakly stratified fluid (point X in Figure 7) with nearly constant shear in the water column. In contrast in strongly stratified layers, very strong shear is generated at or below the base of the mixed layer (Figures 6d–6f). The areas of strong shear for M2 and S2 harmonics are situated in the Laptev Sea and near the entrances to the Arctic Ocean, Yermak Plateau, and the Barents Sea (see Figures 6b and 6c). The locations, variability, and the form of the tidal profiles are consistent with observations in the Laptev Sea [Dmitrenko *et al.*, 2012; Lenn *et al.*, 2011; Janout and Lenn, 2014]. These studies considered different hypotheses for the sporadic increase in mixing in intermediate strongly stratified layers: ice-tide interaction, spring-neap tidal shear enhancement, and interaction with mean currents. Our multidecadal simulations reveal some of the strongest tidal effects on the AO circulation in the Laptev Sea (Figure 14), where mixing of fresh water river runoff with ambient saltier waters results in the modification of water masses.

Another important region of tidal mixing effects is the Yermak Plateau north of Svalbard, where internal tides of diurnal, semidiurnal, and quarter-diurnal periods have been observed [Padman and Dillon, 1991, 1992; Fer *et al.*, 2010]. Our model does produce strong shear in this region, which cannot be explained by internal tides. Internal tides at latitudes above critical are thought to have properties of nonlinear mixed lee waves with the length scales of about 1.5 km [Vasenko *et al.*, 2003], which are not resolved by this model. In these simulations, we find the strongest changes in the turbocline depths, ocean to ice heat flux and resulting changes in the ice thickness both in the short-term (see Figure 11) and the long-term (Figure 14) simulations occurring between the critical latitudes of M2 and S2.

In hypothesis (D), we suggested that rectified tidal currents can significantly affect water mass exchange and ice in the AO. Typically being localized over variations in topographic relief, this process is characterized

by intense quasi-steady vertical motions of isopycnals that can push warm AW toward the surface or bottom boundary layers and cause further entrainment of AW into the mixed layers. The regions of strongest bottom vertical Ekman pumping resulting in geostrophic motions of isopycnals and ageostrophic quasi-steady motions due to tidal vorticity stretching correspond to the gateways of AW to the Arctic Ocean and concentrate at the shelf break regions (Figure 9) and collocate with the regions of strong tidal shear. In the 1 year runs with and without tides, we find that tides are responsible for an increase in the magnitude of the vertical displacement of isopycnals by 50% near the seabed (Figure 10e). The model also demonstrates stronger vertical monthly mean motions in the tidal case (Figures 12 and 13). When ice forms, additional tidal-induced surface Ekman vertical motions arise at the ice-ocean interface, due to horizontal variations of tidal currents and ice-ocean shear stresses over rough topography (see Figure 13).

Polyakov et al. [2012] and *Lenn et al.* [2009] argue that observed transformation of AW along Eurasian shelf break could not be explained by relatively low double-diffusive mixing. *Rippeth et al.* [2015] observed an enhanced dissipation rate of turbulent kinetic energy in several isolated locations: in the vicinity of the Yermak Plateau and above the shelf-break of the Laptev and East-Siberian Seas. That study suggested tides as a main mechanism for the turbulent energy dissipation. All the observed regions in the above studies were characterized by steep seabed topography, and the high level of dissipation rate was strongly correlated with the bathymetric slopes and tidal dissipation rates. Therefore, it has been proposed that short and non-linear internal tides are responsible for the enhanced turbulence and dissipation rate. While our model does not resolve internal tides, these locations (Yermak Plateau, shelf-break of the Laptev Sea and Siberian Seas) correspond to the area of both strong shear in the tidal currents (Figures 6b and 6c) and tidally induced quasi-steady vertical motions (Figures 9c and 9d). A combination of these effects could provide an alternative mechanism (to internal tides), explaining the strong modification of Atlantic Waters along the Eurasian shelf break.

Comparing the long-term simulations with and without tides shows stronger fronts, relatively colder AW, sharper isotherms/isohalines and outcropping of isopycnals in the simulation with tides at the locations of strong vertical bottom Ekman pumping. These processes, i.e., thicker mixed layers, lateral and vertical rectified currents, concentrated at the shelf break can significantly modify shelf edge-deep ocean exchange, including dense water cascades, modification of AW by cold and saltier Barents Sea waters, and cascading processes. Simulations with tides (see Figure 16) show significantly colder, and slightly fresher near-bottom waters across the Barents and Kara Sea shelves. The observed locations of cascading [*Ivanov et al.*, 2004, Figure 32] correspond to the locations of vertical bottom pumping and tidally induced rectified currents, shown in Figures 9a–9d.

We conclude that tidal shear stresses at the bottom and the ice-ocean interface facilitate the transport of warmer and saltier AW to the surface layers, while the effects of tides along the Siberian shelf result in mixing of fresh river runoff waters with saltier water below the eroding halocline. Mixed layers, being much thicker due to the effects of the critical latitude on the clockwise component of tidal currents, entrain saltier waters to the surface boundary layers. Along the Siberian coast with strong river runoff, thicker boundary layers result in mixing in halocline and penetration of freshened waters to depth. Finally we find that, in this particular model, tides are responsible for ~15% of the ice volume reduction and the presence of more salt waters at the surface in average by ~1–1.7 PSU (Figure 14). Tides significantly modify the freshwater pathways along the Siberian shelf, resulting in saltier water along the Greenland coast. Tides affect the fresh water and heat content in the AO, with a reduction in the former by 7% in the upper 100 m.

Some coarse resolution global ocean models already include the effect of unresolved tides [e.g., *Canuto et al.*, 2010] through the application of the Monin-Obukhov law in a stratified fluid, and shear stresses and enhanced bottom drag calculated from tidal velocities. However, the Monin-Obukhov law does not contain the inertial and tidal frequencies as governing parameters. Our study shows that effect of tides on mixing and mixed layer depths is strong at high latitudes near to the critical latitudes of semidiurnal tides. Similar effects are also observed at midlatitudes near to the critical latitudes of diurnal tides (~30°). *Souza* [2013] has explored a way to parameterize the effects of thick Ekman layer depth on the clockwise component of currents (i.e., combined effect of rotation and tidal frequency) and stratification on the water column structure in shallow shelf seas. However, the accurate representation of mixing processes in global models requires additional efforts to develop observation-based or model-based parameterization of mixed layer in the tidal seas.

In principle, the effect of baroclinic tides can also be accounted for in coarse resolution models by incorporating seasonally calculated 3-D amplitudes and phases of tidal shear from a fine-resolution tidal baroclinic model into the mixing parameterization. Moreover, several of the climate models under development for future IPCC assessments have similar resolution to that used in the present study. For example, the ocean component of the new UKESM1 model uses the 1/4° global model that forms the basis for the model used in this study. This opens the possibility for tidal effects to be simulated directly in coupled ocean-atmosphere climate models, accepting the need to explore their impact more widely than the AO in such a model.

In summary, this study demonstrates that including tidal dynamics has an impact on the sea ice and water masses in AO and improves the modeling of the current state of the Arctic sea ice. This study provides evidence that including key shelf-sea physical processes, currently absent in climate models, either explicitly or as parameterizations will improve the fidelity of the forward simulations and, therefore, increasing our confidence in future climate projections.

Appendix A: Estimate of the Mean Ice Tidal Shear

Kowalik and Proshutinsky [1994] proposed to use a maximal shear, D , of ice velocity as a measure of ice cover deformation expressed through the tensors of horizontal tension/compression strain rate D_T and of shear strain rate D_S .

$$D^2 = D_T^2 + D_S^2. \tag{A1}$$

However, from their paper, it is not clear how they estimated the integral effect over all the tidal harmonics. In this study, we estimate mean maximal ice velocity shear by the summation of tidal mean D^2 over all $n = (1:m)$ harmonics:

$$D^2 = \sum_{n=1}^m \{D_{T,n}^2 + D_{S,n}^2\}; \quad \{x_n\} = T_n^{-1} \int_0^{T_n} x_n dt, \tag{A2}$$

where curled brackets $\{x_n\}$ denote averaging of variable, x_n , over tidal period, T_n , n denotes a tidal constituent. In the curvilinear coordinates

$$D_T = e_2(u/e_2)_x - e_1(v/e_1)_y \text{ and } D_S = e_1(u/e_1)_y + e_2(v/e_2)_x, \tag{A3}$$

where e_1 and e_2 and are horizontal scale factors in the x and y directions of coordinate system and u , v are the components of velocity. Substituting the expressions for tidal velocities:

$$u = u_t = U \cos(\omega t + \varphi_u); \quad v = v_t = V \cos(\omega t + \varphi_v)$$

(where t is time, ω is frequency of tidal constitute, φ_u , φ_v are phases of the velocity components) to (A1), (A2) and integrating over tidal period $2\pi/\omega$ we get the expression for the mean squared ice velocity shear:

$$\begin{aligned} \{D^2\} = & 0.5 \left([e_2(U/e_2)_x]^2 + [e_1(V/e_1)_y]^2 + [e_1(U/e_1)_y]^2 + [e_2(V/e_2)_x]^2 \right) + \\ & \cos(\varphi_u - \varphi_v) (e_1 e_2 (U/e_1)_y (V/e_2)_x - e_1 e_2 (U/e_2)_x (V/e_1)_y) + UV(\varphi_u)_y (\varphi_v)_x - \\ & UV(\varphi_u)_x (\varphi_v)_y + \sin(\varphi_u - \varphi_v) (e_1 (U/e_1)_y V(\varphi_v)_x - e_2 (V/e_2)_x U(\varphi_u)_y - e_2 (U/e_2)_x V(\varphi_v)_y \\ & + e_1 (V/e_1)_y U(\varphi_u)_x). \end{aligned} \tag{A4}$$

Appendix B: Equations for Mean Ocean Velocity, Vorticity, and Estimates of Tidal-Induced Vertical Motions in the Tidal Sea

B1. Equation for Mean Velocity in the Tidal Seas

Let us decompose velocity components in to the slow-varying (synoptic, seasonal, etc.) and high-frequency tidal components of motion:

$$\mathbf{u} = \mathbf{u}_\tau + \mathbf{u}_t, \quad \{\mathbf{u}_t\} = \int_0^T \mathbf{u}_t dt = 0,$$

where subscripts τ and t denote “mean” and tidal components, respectively, $\{\}$ denotes averaging over tidal period T . Averaging the equations of motion over tidal period we obtain

$$\begin{aligned} \partial_\tau \mathbf{u}_\tau + (f \mathbf{e}_z + \nabla_H \times \mathbf{u}_\tau) \times \mathbf{u}_\tau + \{ (\nabla_H \times \mathbf{u}_t) \times \mathbf{u}_t \} = \\ - \nabla_H (g\eta + KE + KET + P) + \partial_z (K_m \partial_z \mathbf{u}_\tau) + \{ \partial_z (K_{mt} \partial_z \mathbf{u}_t) \} + DIFF_H \end{aligned} \quad (B1)$$

where f is a Coriolis parameter, $KE = (u_\tau^2 + v_\tau^2)/2$ and $KET = \{u_t^2 + v_t^2\}/2$ are kinetic energy of the mean and tidal currents, $DIFF_H$ denotes lateral mixing term, K_m and K_{mt} are time mean and fluctuating components of vertical turbulent viscosity, \mathbf{e}_z is the unit vector in vertical direction, η is surface height, P is baroclinic pressure, f is Coriolis acceleration, and ∇_H is horizontal gradient operator. Additional terms I and II are the effects of tidal Reynolds stresses: due to vorticity, generated over topographic anomalies and the potential term. Terms III and IV are the effects of tidal shear and tidally induced mixing. Mean diffusivity K_m itself contains tidally induced component due to enhance of shear production of turbulent kinetic energy due to tides.

At the bottom of the ocean, the boundary conditions for velocity are set by a quadratic friction law (in this particular model with an asymptotic of the logarithmic boundary layer):

$$\boldsymbol{\tau}_{bot} = -\rho(K_m + K_{mt})(\partial_z \mathbf{u}_\tau + \partial_z \mathbf{u}_t) = -\rho C_{db} |\mathbf{u}_\tau + \mathbf{u}_t| (\mathbf{u}_\tau + \mathbf{u}_t), \quad (B2)$$

where C_{db} is seabed drag coefficient and ρ is the density of water.

At the ice-ocean interface, shear stress $\boldsymbol{\tau}_{io}$ is correspondingly:

$$\boldsymbol{\tau}_{io} = -\rho(K_m + K_{mt})[\partial_z \mathbf{u}_{ts} + K_{mt} \partial_z \mathbf{u}_t] = -\rho C_{dio} |\mathbf{u}_s - \mathbf{u}_i| (\mathbf{u}_s - \mathbf{u}_i), \quad (B3)$$

where $\mathbf{u}_i = \mathbf{u}_{it} + \mathbf{u}_{it}$ is ice velocity, which contains both tidal \mathbf{u}_{it} and slow-varying components \mathbf{u}_{it} . C_{dio} is the drag coefficient between sea ice and ocean, subscript “s” denotes surface values. Tidal mean ice-ocean and bottom shear magnitude and direction cannot be found analytically in a general case.

B2. Equation for the Mean Vorticity and Estimates of Tidal-Induced Vertical Motions

Similarly, using the equation of vorticity [see e.g., Gill, 1982] and again decomposing variables into tidal and mean (i.e., slow-varying component) components we get

$$\begin{aligned} \partial_\tau \zeta_\tau + \mathbf{u}_\tau \cdot \nabla (\zeta_\tau + f) - f \partial_z w_\tau - \mathbf{e}_z \cdot \partial_z \mathbf{u}_\tau \times \nabla w_\tau - \nabla \times \partial_z (K_m \partial_z \mathbf{u}_\tau) = \\ \{ \mathbf{u}_t \cdot \nabla \zeta_t \} + \{ \zeta_t \partial_z w_t \} - \{ \mathbf{e}_z \cdot \partial_z \mathbf{u}_t \times \nabla w_t \} + \nabla \times \{ \partial_z (K_{mt} \partial_z \mathbf{u}_t) \}. \end{aligned} \quad (B4)$$

In a steady state case on an f-plane and with assumptions of smallness of time-mean relative vorticity ζ_τ in comparison with planetary, $\zeta_\tau = \nabla_H \times \mathbf{u}_\tau \ll f$; and smallness of the mean component of current in comparison with the tidal component, $|\mathbf{u}_\tau| \ll |\mathbf{u}_t|$; we get the equation for the estimation of vertical velocity:

$$\begin{aligned} -f \partial_z w_\tau - \nabla \times \partial_z (K_m \partial_z \mathbf{u}_\tau) = \\ \{ \mathbf{u}_t \cdot \nabla \zeta_t \} + \{ \zeta_t \partial_z w_t \} - \{ \mathbf{e}_z \cdot \partial_z \mathbf{u}_t \times \nabla w_t \} + \nabla \times \{ \partial_z (K_{mt} \partial_z \mathbf{u}_t) \}, \end{aligned} \quad (B5)$$

where in absence of tides, the left-hand side corresponds to the Ekman balance at steady state. Terms I–III are production terms due to advection of relative vorticity of tidal currents, stretching and tilting of horizontal relative vorticity into vertical, IV is tidally induced Ekman pumping term. Term IV is important only near seabed and at the ocean-ice boundary layers and gives the following estimates of vertical velocity production. Integrating over the Ekman bottom and surface depth, we get the Ekman vertical fluxes to the interior:

$$w_{et}^{bot} = (\nabla_H \times \boldsymbol{\tau}_{bot}) / (\rho f). \quad (B6)$$

$$w_{et}^{surf} = -(\nabla_H \times \boldsymbol{\tau}_{iot}) / (\rho f). \quad (B7)$$

Estimates of tilting and stretching terms are

$$w_t^{tilt}(z) = - \int_{-h}^z \{ \mathbf{k} \cdot \partial_z \mathbf{u}_t \times \nabla w_t \} dz / f. \quad (B8)$$

$$w_t^{str}(z) = \int_{-h}^z \{\zeta_t \partial_z w_t\} dz / f. \tag{B9}$$

$$w_t^{adv}(z) = \int_{-h}^z \{\mathbf{u}_t \cdot \nabla \zeta_t\} dz / f. \tag{B10}$$

(B6)–(B10) are only approximations of the actual strength of vertical motions, or production terms of vertical velocity. However, tidally induced persistent vertical motions can be reconstructed using, for example, omega-type [Sanz and Viúdez, 2005; Giordani et al., 2006] or Sawyer-Eliassen [Clayson et al., 2008] semigeostrophic equations with corresponding tidally induced source terms included on the right-hand side of the equation.

B3. Estimates of Vertical Velocity Induced by Stretching Term

Let us estimate w_t^{str} as

$$w_t^{str} = \int_{-h}^z \{\zeta_t \partial_z w_t\} dz / f \approx \{\zeta_t w_t\} / f. \tag{B11}$$

Substituting to (B11) expressions for tidal velocity as

$$u_t = U \cos(\omega t + \varphi_u); \quad v_t = V \cos(\omega t + \varphi_v); \quad w_t = W \cos(\omega t + \varphi_w).$$

We get

$$w_t^{str} \approx 0.5W(\partial_x(V e_2)/e_2 * \cos(\varphi_w - \varphi_v) - \partial_y(U e_1)/e_1 * \cos(\varphi_w - \varphi_u) + V \partial_x \varphi_v \sin(\varphi_w - \varphi_v) - U \partial_y \varphi_u \sin(\varphi_w - \varphi_u)) / f. \tag{B12}$$

Finally, w_t^{str} is found as a sum of all tidal harmonics.

Acknowledgments

The authors thank Laurie Padman (Earth and Space Research) and anonymous reviewers for their very important and valuable comments that allow us significantly to improve this paper. The authors acknowledge the National Capability funding provided by the UK Natural Environment Research Council (NERC) and the NERC Ocean Acidification Programme (ROAM, NERC grant NE/H01732/1). The study is also a contribution to the TEA-COSI Project of the UK Arctic Research Programme (NERC grant NE/I028947/), the Forum for Arctic Ocean Modeling and Observational Synthesis (FAMOS), funded by the National Science Foundation Office of Polar Programs, awards PLR-1313614 and PLR-1203720. Model data from this work will be made available from the British Oceanographic Data Centre (BODC, <http://www.bodc.ac.uk/>). The ORCA simulations use as a boundary and initial conditions were completed as part of the DRAKKAR collaboration [Barnier et al., 2006]. We also acknowledge the use of the UK National High Performance Computing resource.

References

- Aksenov, Y., S. Bacon, A. C. Coward, and A. J. G. Nurser (2010), The North Atlantic inflow to the Arctic Ocean: High resolution model study, *J. Mar. Syst.*, 79(1–2), 1–22, doi:10.1016/j.jmarsys.2009.05.003.
- Aksenov, Y., V. V. Ivanov, A. J. G. Nurser, S. Bacon, I. V. Polyakov, A. C. Coward, A. C. Naveira-Garabato, and A. Beszczynska-Moeller (2011), The Arctic Circumpolar Boundary Current, *J. Geophys. Res.*, 116, C09017, doi:10.1029/2010JC006637.
- Anderson, L. G., G. Björk, O. Holby, E. P. Jones, G. Kattner, K.-P. Koltermann, B. Liljeblad, R. Lindegren, B. Rudels, and J. H. Swift (1994), Water masses and circulation in the Eurasian Basin: Results from the Oden 91 Expedition, *J. Geophys. Res.*, 99(C2), 3273–3283.
- Bacon, S., A. Marshall, N. P. Holliday, Y. Aksenov, and S. R. Dye (2014), Seasonal variability of the East Greenland Coastal Current, *J. Geophys. Res.*, 119, 3967–3987, doi:10.1002/2013JC009279.
- Barnier, B., et al. (2006), Impact of partial steps and momentum advection schemes in a global ocean circulation model at eddy permitting resolution, *Ocean Dyn.*, 56, 543–567, doi:10.1007/s10236-006-0082-1.
- Bouillon, S., M. A. M. Maqueda, V. Legat, and T. Fichefet (2009), An elastic-viscous-plastic sea ice model formulated on Arakawa B and C grids, *Ocean Modell.*, 27, 174–184.
- Brodeau, L., B. Barnier, A. M. Treguier, T. Penduff, S. Gulev (2010), An ERA40-based atmospheric forcing for global ocean circulation models, *Ocean Modell.*, 31, 88–104, doi:10.1016/j.ocemod.2009.10.005.
- Burchard, H., and T. P. Rippeth (2009), Generation of bulk shear spikes in a shallow stratified tidal seas, *J. Phys. Oceanogr.*, 39, 969–985.
- Canuto, V. M., A. M. Howard, Y. Cheng, C. J. Muller, A. Lebbosier, and S. R. Jayne (2010), Ocean turbulence, III: New GISS vertical mixing scheme, *Ocean Modell.*, 34, 70–91, doi:10.1016/j.ocemod.2010.04.006.
- Chen, C., G. Gao, J. Qi, A. Proshutinsky, R. C. Beardsley, H. Lin, G. Cowles, and H. Huang (2009), A new high-resolution unstructured grid finite-volume Arctic Ocean model (AO-FVCOM). An application for tidal studies, *J. Geophys. Res.*, 114, C08017, doi:10.1029/2008JC004941.
- Clayson, C. A., M. Luneva, and P. Cunningham (2008), Downwelling and upwelling regimes: Connection between surface fronts and abyssal circulation, *Dyn. Atmos. Oceans*, 45, 165–186.
- Colella, P., and P. R. Woodward (1984), Piecewise Parabolic Method (PPM) for gas-dynamical simulations, *J. Comput. Phys.*, 54(1), 174–201.
- Colony, R., and A. S. Thorndike (1980), The horizontal coherency of the motion of summer sea ice, *J. Phys. Oceanogr.*, 10(8), 1281–1289.
- Dmitrenko, I. A., S. A. Kirillov, E. Bloskhina, and Y.-D. Lenn (2012), Tide-induced vertical mixing in the Laptev Sea coastal polynya, *J. Geophys. Res.*, 117, C00G14, doi:10.1029/2011JC006966.
- Dmitrenko, I. A., et al. (2014), Heat loss from the Atlantic water layer in the northern Kara Sea: Causes and consequences, *Ocean Sci.*, 10, 719–730, doi:10.5194/os-10-719-2014.
- Dosser, H. V., L. Rainville, and J. M. Toole (2014), Near-inertial internal wave field in the Canada Basin from ice-tethered profilers, *J. Phys. Oceanogr.*, 44(2), 413–426.
- Duchez, A., E. Frajka-Williams, N. Castro, J. Hirschi, and A. Coward (2014), Seasonal to interannual variability in density around the Canary Islands and their influence on the Atlantic meridional overturning circulation at 26 N, *J. Geophys. Res. Oceans*, 119, 1843–1860, doi:10.1002/2013JC009416.
- Egbert, D. G., and S. Y. Erofeeva (2002), Efficient inverse modelling of barotropic ocean tides, *J. Ocean. Atmos. Technol.*, 19, 182–204.
- Fer, I., R. Skogseth, and F. Geyer (2010), Internal waves and mixing in the marginal ice zone near Yermak Plateau, *J. Phys. Oceanogr.*, 40, 1613–1630.
- Fichefet, T., and M. A. M. Maqueda (1997), Sensitivity of a global sea ice model to the treatment of ice thermodynamics and dynamics, *J. Geophys. Res.*, 102(C6), 12,609–12,646.

- Francis, J. A., and S. J. Vavrus (2012), Evidence linking Arctic amplification to extreme weather in mid-latitudes, *Geophys. Res. Lett.*, *39*, L06801, doi:10.1029/2012GL051000.
- Furevik, T., and A. Foldvik (1996), Stability of M_2 critical latitude in the Barents Sea, *J. Geophys. Res.*, *101*(C4), 8823–8837.
- Giles, K. A., S. W. Laxon, A. L. Ridout, D. J. Wingham, and S. Bacon (2012), Western Arctic Ocean freshwater storage increased by wind-driven spin-up of the Beaufort Gyre, *Nat. Geosci.*, *5*, 194–197, doi:10.1038/ngeo1379.
- Gill, A. E. (1982), *Atmosphere-Ocean Dynamics*, 662 pp., Academic, N. Y.
- Giordani, H., L. Prieur, and G. Caniaux (2006), Advanced insights into sources of vertical velocity in the ocean, *Ocean. Dyn.*, *56*, 513–524.
- Heil, P., and W. D. Hibler III (2002), Modeling the high frequency of ice sea drift and deformation, *J. Phys. Oceanogr.*, *32*, 3039–3057.
- Hibler, W. D., III, W. F. Weeks, A. Kovacs, and S. F. Ackley (1974), Differential sea ice drift. I: Spatial and temporal variations in sea ice deformation, *J. Glaciol.*, *31*, 437–455.
- Holloway, G., and A. Proshutinsky (2007), Role of tides in Arctic Ocean/ice climate, *J. Geophys. Res.*, *112*, C04S06, doi:10.1029/2006JC003643.
- Howarth, M. J. (1998), The effects of stratification on tidal current profiles, *Cont. Shelf Res.*, *18*, 1235–1254.
- Hunke, E. C., and J. K. Dukowicz (1997), An elastic-viscous-plastic model for sea ice dynamics, *J. Phys. Oceanogr.*, *27*, 1849–1867.
- Hunkins, K. (1967), Inertial oscillations of Fletchers Ice Island (T-3), *J. Geophys. Res.*, *72*(4), 1165–1174.
- Huthnance, J. M. (1981), On mass transports generated by tides and long waves, *J. Fluid Mech.*, *102*, 367–387, doi:10.1017/S0022112081002693.
- Ivanov, V. V., G. I. Shapiro, J. M. Huthnance, D. L. Aleynik, and P. N. Golovin (2004), Cascades of dense water around the world ocean, *Prog. Oceanogr.*, *60*, 47–98.
- Jahn, A., et al. (2012), Arctic Ocean freshwater: How robust are model simulations?, *J. Geophys. Res.*, *117*, C00D16, doi:10.1029/2012JC007907.
- James, I. D. (2000), A high-performance explicit vertical advection scheme for ocean models: How PPM can beat the CFL condition, *Appl. Math. Modell.*, *24*, 1–9.
- Janout, A. M., and Y.-D. Lenn (2014), Semidiurnal Tides on the Laptev Sea Shelf with Implications for Shear and Vertical Mixing, *J. Phys. Oceanogr.*, *44*, 202–219.
- Johnson, M., et al. (2012), Evaluation of Arctic sea ice thickness simulated by Arctic Ocean Model Intercomparison Project models, *J. Geophys. Res.*, *117*, C00D13, doi:10.1029/2011JC007257.
- Kantha, L. H., and C. A. Clayson (1994), An improved mixed layer model for geophysical applications, *J. Geophys. Res.*, *99*(C12), 25,235–25,266.
- Koentopp, M., O. Eisen, C. Kottmeier, L. Padman, and P. Lemke (2005), Influence of tides on sea ice in the Weddell Sea: Investigations with a high-resolution dynamic-thermodynamic sea ice model, *J. Geophys. Res.*, *110*, C02014, doi:10.1029/2004JC002405.
- Kowalik, Z., and A. Y. Proshutinsky (1993), Diurnal tides in the Arctic Ocean, *J. Geophys. Res.*, *98*, 0148–0227, doi:10.1029/93JC01363.
- Kowalik, Z., and A. Yu. Proshutinsky (1994), The Arctic Ocean tides, in *The Polar Oceans and Their Role in Shaping the Global Environment*, *Geophys. Monogr. Ser.*, vol. 85, pp. 137–158, AGU, Washington, D. C.
- Kowalik, Z., and A. Yu. Proshutinsky (1995), Topographic enhancement of tidal motion in the western Barents Sea, *J. Geophys. Res.*, *100*(C2), 2613–2637.
- Kwok, R., G. F. Cunningham, and W. D. Hibler III (2003), Sub-daily sea ice motion and deformation from RADARSAT observations, *Geophys. Res. Lett.*, *30*(23), 2218, doi:10.1029/2003GL018723.
- Large, W. G., and S. G. Yeager (2004), Diurnal to decadal global forcing for ocean and sea-ice models: The data sets and flux climatologies, Tech. Rep. TN-460+STR, 105 pp., CGT Division, Nat. Cent. Atmos. Res., doi:10.5065/D6KK98Q6.
- Lenn, Y.-D., P. J. Wiles, S. Torres-Valdes, E. P. Abrahamson, T. P. Rippeth, J. H. Simpson, S. Bacon, S. W. Polyakov, V. Ivanov, and S. Kirillov (2009), Vertical mixing at intermediate depths in the Arctic boundary current, *Geophys. Res. Lett.*, *36*, L05601, doi:10.1029/2008GL036792.
- Lenn, Y.-D., T. P. Rippeth, C. P. Old, S. Bacon, I. Polyakov, V. Ivanov, and J. Hollemann (2011), Intermittent intense turbulent mixing under ice in the Laptev Sea continental Shelf, *J. Phys. Oceanogr.*, *41*(3), 531–547.
- Loder, J. W. (1980), Topographic rectification of tidal currents on the sides of Georges Bank, *J. Phys. Oceanogr.*, *10*, 1399–1416.
- Maas, L. R., and J. J. van Haren (1987), Observation on the vertical structure of tidal and inertial currents in the central North Sea, *J. Mar. Res.*, *45*, 293–318.
- MacAyeal, D. R. (1985), Tidal rectification below the Ross Ice Shelf, Antarctica, *Oceanol. Antarct. Cont. Shelf*, *43*, 109–132.
- Mack, S., L. Padman, and J. Klinck (2013), Extracting tidal variability of sea ice concentration from AMSR-E passive microwave single-swath data: A case study of the Ross Sea, *Geophys. Res. Lett.*, *40*, 547–552, doi:10.1002/grl.50128.
- Madec, G., and NEMO Team (2008), NEMO Ocean Engine, *Note du Pole de modélisation* 27, 211 pp., Inst. Pierre-Simon Laplace, France, ISSN 1288-1619. [Available at http://www.nemo-ocean.eu/content/download/11245/56055/file/NEMO_book_v3_2.pdf.]
- Makinson, K. (2002), Modeling tidal current profiles and vertical mixing beneath Filchner-Ronne Ice Shelf, Antarctica, *J. Phys. Oceanogr.*, *32*(1), 202–215.
- Makinson, K., P. R. Holland, A. Jenkins, K. W. Nicholls, and D. M. Holland (2011), Influence of tides on melting and freezing beneath Filchner-Ronne Ice Shelf, Antarctica, *Geophys. Res. Lett.*, *38*, L06601, doi:10.1029/2010GL046462.
- Makinson, K., M. Schröder, and S. Østerhus (2006), Effect of critical latitude and seasonal stratification on tidal current profiles along Ronne Ice Front, Antarctica, *J. Geophys. Res.*, *111*, C03022, doi:10.1029/2005JC003062.
- Martini, K. I., H. L. Simmons, C. A. Stoudt, and J. K. Hutchings (2014), Near-inertial internal waves and sea ice in the Beaufort Sea, *J. Phys. Oceanogr.*, *44*(8), 2212–2234, doi:10.1175/JPO-D-13-0160.1.
- McClimans, T. A., and J. H. Nilssen (1993), Laboratory simulation of the ocean currents in the Barents Sea, *Dyn. Atmos. Oceans*, *19*, 3–36.
- Metzger, E. J., et al. (2014), US Navy operational global ocean and Arctic ice prediction systems, *Oceanography*, *27*(3), 32–43, doi:10.5670/oceanog.2014.66.
- Nøst, E. (1994), Calculating tidal current profiles from vertically integrated models near the critical latitude in the Barents Sea, *J. Geophys. Res.*, *99*(C4), 7885–7901.
- Nurser, A. J. G., and S. Bacon (2014), The Rossby radius in the Arctic Ocean, *Ocean Sci.*, *10*, 967–975, doi:10.5194/os-10-967-2014.
- O’Dea, et al. (2012), An operational ocean forecast system incorporating SST data assimilation for the tidally driven European North-West European shelf, *J. Oper. Oceanogr.*, *5*, 3–17.
- Padman, L., and T. M. Dillon (1987), Vertical heat fluxes through the Beaufort Sea thermohaline staircase, *J. Geophys. Res.*, *92*(C10), 10,799–10,806.
- Padman, L., and T. M. Dillon, (1991), Turbulent mixing near the Yermak Plateau during the Coordinated Eastern Arctic Experiment, *J. Geophys. Res.*, *96*(C3), 4769–4782.
- Padman, L., and S. Erofeeva (2004), A barotropic inverse tidal model for the Arctic Ocean, *Geophys. Res. Lett.*, *31*, L02303, doi:10.1029/2003GL019003.

- Padman, L., A. J. Plueddemann, R. D. Muench, and R. Pinkel (1992), Diurnal tides near the Yermak Plateau, *J. Geophys. Res.*, *97*(C8), 12,639–12,652.
- Pease, C. H., P. Turet, and R. S. Pritchard (1995), Barents Sea tidal and inertial motion from ARGOS ice buoys during the coordinated eastern Arctic experiment, *J. Geophys. Res.*, *100*(C12), 24,705–24,718.
- Penduff, T., J. Le Sommer, B. Barnier, A.-M. Treguier, J.-M. Molines, and G. Madec (2007), Influence of numerical schemes on current-topography interactions in 1/4° global ocean simulations, *Ocean Sci.*, *3*, 509–524.
- Perkin, R. G., and E. L. Lewis (1984), Mixing in the West Spitsbergen Current, *J. Phys. Oceanogr.*, *14*, 1315–1325.
- Pinkel, R. (2005), Near-inertial wave propagation in the Western Arctic, *J. Phys. Oceanogr.*, *35*, 645–665.
- Pithan, F., and T. Mauritsen (2014), Arctic amplification dominated by temperature feedbacks in contemporary climate models, *Nat. Geosci.*, *7*, 181–184, doi:10.1038/ngeo2071.
- Polton, J. A. (2015), Tidally induced mean flow over bathymetric features: A contemporary challenge for high-resolution wide-area models, *Geophys. Astrophys. Fluid Dyn.*, *109*, 207–215, doi:10.1080/03091929.2014.952726.
- Polyakov, I. V., et al. (2012), Arctic warming contributes to reduces polar cap, *J. Phys. Oceanogr.*, *40*, 2743–2756.
- Popova, E. E., A. Yool, Y. Aksenov, and A. C. Coward (2013), Role of advection in Arctic Ocean lower trophic dynamics: A modeling perspective, *J. Geophys. Res. Oceans*, *118*, 1571–1586, doi:10.1002/jgrc.20126.
- Postlethwaite, C. F., M. A. Morales Maqueda, V. le Fouest, G. R. Tattersall, J. T. Holt, and A. J. Willmott (2011), The effect of tides on dense water formation in Arctic shelf seas, *Ocean Sci.*, *7*, 203–217, doi:10.5194/os-7-203-2011.
- Prandle, D. (1982), The vertical structure of tidal currents, *Geophys. Astrophys. Fluid Dyn.*, *22*, 29–49.
- Prinsenberg, S. J., and E. B. Bennett (1989), Vertical variations of tidal currents in shallow land fast ice-covered regions, *J. Phys. Oceanogr.*, *19*, 1268–1278.
- Proshutinsky, A., R. Krishfield, M.-L. Timmermans, J. Toole, E. Carmack, F. McLaughlin, W. J. Williams, S. Zimmermann, M. Itoh, and K. Shimada (2009), Beaufort Gyre freshwater reservoir: State and variability from observations, *J. Geophys. Res.*, *114*, C00A10, doi:10.1029/2008JC005104.
- Proshutinsky, A. Y., and M. A. Johnson (1997), Two circulation regimes of the wind-driven Arctic Ocean, *J. Geophys. Res.*, *203*(C6), 12,493–12,514.
- Rabe, B., M. Karcher, U. Schauer, J. M. Toole, R. A. Krishfield, S. Pisarev, F. Kauker, R. Gerdes, and T. Kikuchi (2011), An assessment of Arctic Ocean freshwater content changes from the 1990s to the 2006–2008 period, *Deep Sea Res., Part I*, *58*, 173–185, doi:10.1016/j.dsr.2010.12.002.
- Rainville, L., and R. A. Woodgate (2009), Observations of internal wave generation in the seasonally ice-free Arctic, *Geophys. Res. Lett.*, *36*, L23604, doi:10.1029/2009GL041291.
- Ray, R. D., and G. D. Egbert (2004), The global S_1 tide, *J. Phys. Res.*, *34*, 1922–1935.
- Rayner, N. A., D. E. Parker, E. B. Horton, C. K. Folland, L. V. Alexander, D. P. Rowell, E. C. Kent, and A. Kaplan (2003), Global analyses of sea surface temperature, sea ice, and night marine air temperature since the late nineteenth century, *J. Geophys. Res.*, *108*(D14), 4407, doi:10.1029/2002JD002670.
- Rippeth, T. R., B. J. Lincoln, Y.-D. Lenn, J. A. M. Green, A. S. Sundfjord, and S. Bacon (2015), Tide-mediated warming of Arctic halocline by Atlantic heat fluxes over rough topography, *Nat. Geosci.*, *8*, 191–194, doi:10.1038/ngeo2350.
- Robertson, R., L. Padman, and G. D. Egbert (1998), Tides in the Weddell Sea, in ocean, ice, and atmosphere: Interactions at the Antarctic continental margin, *Antarct. Res. Ser.*, *75*, 341–369.
- Robinson, I. S. (1981), Tidal vorticity and residual circulation, *Deep Sea Res., Part A*, *28*(3), 195–212.
- Rudels, B., G. Björk, R. D. Muench, and U. Schauer (1999), Double-diffusive layering in the Eurasian Basin of the Arctic Ocean, *J. Mar. Sys.*, *21*, 3–27.
- Sanz, E. P., and Á. Viúdez (2005), Diagnosing mesoscale vertical motion from horizontal velocity and density data, *J. Phys. Oceanogr.*, *35*, 1744–1762.
- Schauer U., H. Loeng, B. Rudels, V. K. Ozhigin, and V. Dieck (2002), Atlantic Water flow through the Barents and Kara Seas, *Deep Sea Res. I*, *49*, 2281–2298.
- Schweiger A., R. Lindsay, J. Zhang, M. Steele, H. Stern, and R. Kwok (2011), Uncertainty in modeled Arctic sea ice volume, *J. Geophys. Res.*, *116*, C00D06, doi:10.1029/2011JC007084.
- Screen, J. A. (2014), Arctic amplification decreases temperature variance in northern mid-to high-latitudes, *Nat. Clim. Change*, *4*, 577–582.
- Shapiro, G., M. Luneva, J. Pickering, and D. Storkey (2013), The effect of various vertical discretization schemes and horizontal diffusion parameterization on the performance of a 3-D ocean model: the Black Sea case study, *Ocean Sci.*, *9*(2), 377–390, doi:10.5194/os-9-377-2013.
- Soulsby, R. L. (1983), The bottom boundary layer of the shelf sea, in *Physical Oceanography of Coastal and Shelf Seas*, edited by B. Johns, pp. 189–266, Elsevier, N. Y.
- Souza, A. J. (2013), The use of Stokes number to explain frictional tidal dynamics and water column structure in shelf seas, *Ocean Sci.*, *9*, 391–398, doi:10.5194/os-9-2013.
- Souza, A. J., and J. H. Simpson (1996), The modification of tidal ellipses by stratification in the Rhine ROFI, *Cont. Shelf Res.*, *16*, 997–1007.
- Steele, M., R. Morley, and W. Ermold (2001), PHC: A global ocean hydrography with a high-quality Arctic Ocean, *J. Clim.*, *14*(9), 2079–2087, doi:10.1175/1520-0442(2001)0142.0.CO;2.
- St-Laurent, P., F. J. Saucier, and J.-F. Dumais (2008), On the modification of tides in a seasonally ice-covered sea, *J. Geophys. Res.*, *113*, C11014, doi:10.1029/2007JC004614.
- Timmermans, M.-L., J. Toole, R. Krishfield, and P. Winsor (2008), Ice-Tethered Profiler observations of double diffusive staircases in the Canada Basin thermocline, *J. Geophys. Res.*, *113*, C00A02, doi:10.1029/2008JC004829.
- Umlauf, L., and H. Burchard (2003), A generic length-scale equation for geophysical turbulence models, *J. Mar. Res.*, *61*, 235–265.
- Vihma, T. (2014), Effects of Arctic Sea ice decline on weather and climate: A review, *Surv. Geophys.*, *35*(5), 1175–1214.
- Vinje, T., H. Jensen, A. S. Johnsen, S. Loset, S. E. Hamran, S. M. Løvas, and B. Erlingsson (1989), *ID AP-89 R/V Lance Deployment, vol. 2, Field Observations and Analysis*, 72 pp., Norsk Polarinstitutt, Oslo.
- Vlasenko, V., N. Stashchuk, K. Hutter, and K. Sabinin (2003), Nonlinear internal waves forced by tides near the critical latitude, *Deep Sea Res., Part I*, *50*(3), 317–338.
- Zimmerman, J. T. F. (1978), Topographic generation of residual circulation by oscillatory (tidal) currents, *Geophys. Astrophys. Fluid Dyn.*, *11*, 35–47.
- Zimmerman, J. T. F. (1980), Vorticity transfer by tidal currents over irregular topography, *J. Mar. Res.*, *30*(4), 601–630.
- Zimmerman, J. T. F. (1981), Dynamics, diffusion and geomorphological significance of tidal residual currents, *Nature*, *29*, 549–555.